Available online at www.sciencedirect.com
SCIENCE DIRECT®
Annals of Physics 321 (2006) 1408–1456
ANNALS of PHYSICS
www.elsevier.com/locate/aop

Effective Lagrangian Approach to pion photoproduction from the nucleon

C. Fernández-Ramírez [a,b,*], E. Moya de Guerra [a,c], J.M. Udías [c]

[a] *Instituto de Estructura de la Materia, CSIC, Serrano 123, E-28006 Madrid, Spain*
[b] *Departamento de Física Atómica, Molecular y Nuclear, Universidad de Sevilla, Apdo, 1065, E-41080 Sevilla, Spain*
[c] *Departamento de Física Atómica, Molecular y Nuclear, Facultad de Ciencias Físicas, Universidad Complutense de Madrid, Avda, Complutense s/n, E-28040 Madrid, Spain*

Received 8 September 2005; accepted 6 February 2006
Available online 4 April 2006

Abstract

We present a pion photoproduction model on the free nucleon based on an Effective Lagrangian Approach (ELA) which includes the nucleon resonances ($\Delta(1232)$, $N(1440)$, $N(1520)$, $N(1535)$, $\Delta(1620)$, $N(1650)$, and $\Delta(1700)$), in addition to Born and vector meson exchange terms. The model incorporates a new theoretical treatment of spin-3/2 resonances, first introduced by Pascalutsa, avoiding pathologies present in previous models. Other main features of the model are chiral symmetry, gauge invariance, and crossing symmetry. We use the model combined with modern optimization techniques to assess the parameters of the nucleon resonances on the basis of world data on electromagnetic multipoles. We present results for electromagnetic multipoles, differential cross-sections, asymmetries, and total cross-sections for all one pion photoproduction processes on free nucleons. We find overall agreement with data from threshold up to 1 GeV in laboratory frame.
© 2006 Elsevier Inc. All rights reserved.

PACS: 25.20.Lj; 13.60.Le; 14.20.Gk; 25.70.Ef

Keywords: Pion photoproduction; Electromagnetic multipoles; Nucleon resonances; Spin-3/2

* Corresponding author. Fax: +34915855184.
E-mail address: cesar@nuc2.fis.ucm.es (C. Fernández-Ramírez).

0003-4916/$ - see front matter © 2006 Elsevier Inc. All rights reserved.
doi:10.1016/j.aop.2006.02.009

1. Introduction

In spite of the fact that Quantum Chromodynamics (QCD) is regarded as the theory of the strong interaction, in the energy regime of the mass of the nucleon and its resonances a perturbative approach is not suitable. Thus, we have to rely on an effective approach if we are interested on the properties of nucleon resonances and processes where they are involved—mainly meson production which is the dominant decay channel. This paper is devoted to pion photoproduction from the nucleon, a classical topic within nuclear and particle physics, which has been proved as one of the best mechanisms to study the nucleon and its resonances as well as to study the role of the pion and resonances in nuclei [1].

The experimental database [2–4] has been enormously increased thanks to the experiments carried out at LEGS (Brookhaven) [5,6] and MAMI (Mainz) [7] where photons are produced through laser backscattering and bremsstrahlung, respectively. Because of this experimental effort, our knowledge of the $\Delta(1232)$ resonance region has been largely increased, though several discrepancies between Mainz and Brookhaven analyses still remain [6]. Polarization observables, differential cross-sections, and electromagnetic multipoles have been measured with a precision not possible a few years ago and a full description of the amplitudes in the $\Delta(1232)$ region is now available. The database is expected to grow significantly once data from current experiments have been analyzed and when data from new laser backscattering facilities as GRAAL (Grenoble) and LEPS (Harima) become available. The last two facilities have started to run recently and operate at higher energies than LEGS. This situation opens a lot of possibilities for research on nucleon resonances.

In the last decades, pion photoproduction has been studied through many models and using various approaches to the description of the nucleon resonances. Among them there are, Breit–Wigner models [8,9], K-matrix [10,11], Effective Lagrangian Approach (ELA) [12–15], dynamical models [16–19], Breit–Wigner plus a Regge-pole type background to take into account the exchange of heavier mesons [20], as well as quark models with pion treated as an elementary particle [21]. Although in one way or another all models are phenomenological, in this paper we adopt ELA method because we consider it appealing in many respects and it is the most suitable approach in the energy range from threshold up to 1 GeV in laboratory frame, where the main low-lying resonances live. This approach has proved to be a quite successful tool to study pion photoproduction at low/threshold energy [22–24] and provides the most natural framework to extend the model to pion electroproduction [12], electromagnetic pion production in composite nuclei [25] and halo nuclei [26], two pion photoproduction [27], meson exchange currents [28], and exclusive $X(\gamma, N\pi)Y$ processes.

In the last years, the Lagrangian description of spin-3/2 resonances has been greatly improved and many pathologies related to the pion–nucleon–resonance and γ–nucleon–resonance interactions have been overcome [29]. This fact, combined with the substantial enlargement of the pion photoproduction database, demands to revisit the topic and to make the most of these advances to improve our knowledge on nucleon resonances and γ–nucleon–resonance vertices as well as on the pion photoproduction process itself.

We focus on the analysis of pion photoproduction process on free nucleons with the aim of establishing a reliable set of coupling constants and achieving an accurate knowledge on nucleon resonances. The latter are needed for further studies of resonances in

nuclear medium as well as to study the structure of the nucleon through its excitations. This requires to develop a pion photoproduction model and to study the parameters of the nucleon resonances within the model for further implementation in the calculations previously mentioned. In this regard, we consider this paper as a first step towards a deeper understanding of the role of the pion and the resonances in more complicated processes. Our model is an improvement of the one in [12] where we have changed the spin-3/2 Lagrangians and explored other variations which allow us to achieve crossing symmetry and a better description of the resonance widths. The elements included in this model are nucleons, pions, photons, ρ and ω mesons, as well as all four star status spin 1/2 and 3/2 nucleon resonances up to 1.7 GeV in Particle Data Group (PDG, in what follows) [30]. Spin-5/2 resonances are not expected to play an important role in the data analysis carried out in this paper and are left to future exploration.

The paper is organized as follows: in Section 2, we provide the basic features such as conventions and normalizations for cross-sections and amplitudes which will be used throughout the article. In Section 3, we describe the full model and its features in detail, stressing crossing symmetry and the spin-3/2 treatment which avoids well-known pathologies of previous models. In Section 4, we show results for multipoles, differential cross-sections, and remaining physical observables. We also provide the reader with all the parameters of the model explaining how they have been determined. In Section 5, we summarize the main conclusions and results.

2. Kinematics, cross-section, and amplitude decomposition

Notation for kinematics is set to $k = (E_\pi, \vec{k})$ for the outgoing pion, $q = (E_\gamma, \vec{q})$ for the incoming photon, $p = (E, \vec{p})$ for the incoming nucleon, and $p' = (E', \vec{p'})$ for the outgoing nucleon. Mandelstam variables are defined as usual [31]

$$s = (p+q)^2 = (p'+k)^2, \tag{1}$$

$$u = (p'-q)^2 = (p-k)^2, \tag{2}$$

$$t = (k-q)^2 = (p-p')^2. \tag{3}$$

The photon polarization vectors in spherical basis are

$$A^\mu_{\lambda_\gamma=\pm1} = \mp\frac{1}{\sqrt{2}}(0, 1, \pm\mathrm{i}, 0). \tag{4}$$

Following conventions and normalization of [31], the differential cross-section can be written in the center of mass (c.m.) reference system as

$$\sigma(\theta) \equiv \frac{\mathrm{d}\sigma}{\mathrm{d}\Omega^*_\pi} = \frac{1}{64\pi^2}\frac{1}{s^*}\frac{k^*}{E^*_\gamma}\overline{|\mathcal{M}|^2}. \tag{5}$$

Whenever a kinematical quantity appears starred it is defined in the c.m. reference frame. In particular, the c.m. absolute values of the photon and the pion momenta are denoted by q^* and k^*, which stand for $|\vec{q^*}|$ and $|\vec{k^*}|$, respectively. The transition probability is

$$\overline{|\mathcal{M}|^2} = \frac{1}{4}\sum_{\lambda_1\lambda_2\lambda_\gamma}|\mathcal{A}_{\lambda_1\lambda_2\lambda_\gamma}|^2, \tag{6}$$

where $\mathcal{A}_{\lambda_1\lambda_2\lambda_\gamma}$ is the invariant amplitude, with photon polarization λ_γ, initial nucleon helicity λ_1, and final nucleon helicity λ_2. We use the following isospin decomposition

$$\mathcal{A} = \chi_2^\dagger(A^0\tau_j + A^-\tfrac{1}{2}[\tau_j,\tau_3] + A^+\delta_{j3})\pi_j\chi_1, \tag{7}$$

where for simplicity we have dropped helicity subindices (another two isospin decompositions are used and are introduced in appendices).

The isospin decomposition can be related to the physical amplitudes

$$\mathcal{A}(\gamma p \to p\pi^0) = A^+ + A^0, \tag{8}$$

$$\mathcal{A}(\gamma n \to n\pi^0) = A^+ - A^0, \tag{9}$$

$$\mathcal{A}(\gamma n \to p\pi^-) = \sqrt{2}(A^0 - A^-), \tag{10}$$

$$\mathcal{A}(\gamma p \to n\pi^+) = \sqrt{2}(A^0 + A^-). \tag{11}$$

For completeness, we specify the conventions adopted throughout this article. Metric tensor: $g^{\mu\nu} \equiv \mathrm{diag}(1,-1,-1,-1)$; Levi-Civitá tensor: $\epsilon_{0123} = 1$, $\epsilon_{123} = 1$; Pauli matrices: $[\tau_j,\tau_k] = 2\epsilon_{jkl}\tau_l$; Dirac–Pauli matrices: $\{\gamma^\mu,\gamma^\nu\} = 2g^{\mu\nu}$, $\gamma^{\mu\nu} = \frac{1}{2}[\gamma^\mu,\gamma^\nu]$, $\gamma^{\mu\nu\alpha} = \frac{1}{2}(\gamma^\mu\gamma^\nu\gamma^\alpha - \gamma^\alpha\gamma^\nu\gamma^\mu)$, $\gamma_5 = \mathrm{i}\gamma_0\gamma_1\gamma_2\gamma_3$; Electromagnetic field: $F^{\mu\nu} = \partial^\mu\hat{A}^\nu - \partial^\nu\hat{A}^\mu$, $\tilde{F}^{\mu\nu} = \frac{1}{2}\epsilon^{\mu\nu\alpha\beta}F_{\alpha\beta}$, where $\hat{A}^\mu$ is the photon field.

3. The model

In this section, we present a complete description of the model and its features. Using as starting point Weinberg's theorem [32], we construct a fully relativistic, chiral symmetric, gauge invariant, and crossing symmetric model based on suitable effective Lagrangians for particle couplings. From these Lagrangians we obtain the invariant amplitudes and physical observables. This procedure has been adopted in many papers, i.e. [12–15], and has been proved to be a successful way to treat the pion photoproduction process. However, previous works had pathologies in the description of the spin-3/2 particles which are not present in our model. The basic idea is to build consistently the most general Lagrangians for vertices, taking into account all possible symmetries (crossing symmetry, gauge invariance, and chiral symmetry), and to use Feynman rules to obtain invariant amplitudes which can be related to physical observables. The model can be split into three different types of contributions: Born terms (Fig. 1), vector mesons exchange (Fig. 2E), and spin-1/2 and spin-3/2 nucleon resonance excitations (Fig. 2F and G). There is no contribution from σ meson exchange because of charge conjugation violation of the $\sigma\pi\gamma$ coupling [11].

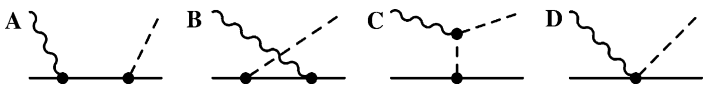

Fig. 1. Feynman diagrams for Born terms: (A) direct or s-channel, (B) crossed or u-channel, (C) pion in flight or t-channel, and (D) Kroll–Rudermann (contact).

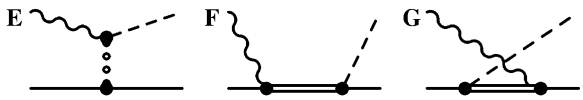

Fig. 2. Feynman diagrams for vector meson exchange (E) and resonance excitations: (F) direct or s-channel and (G) crossed or u-channel.

We consider that all the relevant degrees of freedom are taken into account except perhaps spin-5/2 resonances. Our choice of Lagrangians is explained and justified in the forthcoming subsections. All the invariant amplitudes can be found in Appendix A.

3.1. Born terms

Born terms are the Feynman diagrams shown in Fig. 1 in which only pions, photons, and nucleons are involved. We start from the free Lagrangians for pions (Klein–Gordon) and nucleons (Dirac) and a phenomenological pion–nucleon interaction. This last interaction is chosen as a pseudovector (PV) coupling to the pion because it is the lowest order in derivatives compatible with the low-energy behavior of the pion and chiral symmetry [22,33]

$$\mathcal{L}_{\pi NN} = \frac{f_{\pi N}}{m_\pi}\bar{N}\gamma_\mu\gamma_5\tau_j\left(\partial^\mu\pi_j\right)N, \tag{12}$$

where m_π is the mass of the pion, $f_{\pi N}$ is the pseudovector coupling constant, and the sign is fixed by phenomenology. According to [34], $f_{\pi N}$ is set to $f_{\pi N}^2/4\pi = 0.0749$. The use of the PV coupling for the pion in our effective Lagrangian grants that low-energy theorems of current algebra and partially conserved axial-vector current (PCAC) hypothesis are incorporated in the model.

The electromagnetic field is included in the usual way by minimal coupling to the photon field ($\partial^\alpha \to \partial^\alpha + \mathrm{i}e\hat{Q}\hat{A}^\mu$; where $\hat{Q}$ is the charge operator) and taking into account phenomenologically the anomalous magnetic moment of the nucleon

$$\mathcal{L} = -\frac{\mathrm{i}e}{4M}F_2^{\mathrm{V}}\bar{N}\frac{1}{2}\left(F_2^{\mathrm{S/V}} + \tau_3\right)\gamma_{\alpha\beta}NF^{\alpha\beta}. \tag{13}$$

$F_2^{\mathrm{S/V}}$ is defined as the ratio between isospin-scalar and isospin-vector form factors ($F_2^{\mathrm{S/V}} \equiv F_2^{\mathrm{S}}/F_2^{\mathrm{V}}$).

The interacting Lagrangian for Born terms is

$$\begin{aligned}\mathcal{L}_{\mathrm{Born}} = &-\mathrm{i}eF_\pi\hat{A}^\alpha\epsilon_{jk3}\pi_j(\partial_\alpha\pi_k) - e\hat{A}^\alpha F_1^{\mathrm{V}}\bar{N}\gamma_\alpha\frac{1}{2}\left(F_1^{\mathrm{S/V}} + \tau_3\right)N \\ &- \mathrm{i}eF_1^{\mathrm{V}}\frac{f_{\pi N}}{m_\pi}\hat{A}^\alpha\bar{N}\gamma_\alpha\gamma_5\frac{1}{2}[\tau_j,\tau_3]\pi_jN \\ &- \frac{\mathrm{i}e}{4M}F_2^{\mathrm{V}}\bar{N}\frac{1}{2}\left(F_2^{\mathrm{S/V}} + \tau_3\right)\gamma_{\alpha\beta}NF^{\alpha\beta} + \frac{f_{\pi N}}{m_\pi}\bar{N}\gamma_\alpha\gamma_5\tau_jN(\partial^\alpha\pi_j),\end{aligned} \tag{14}$$

where e is the absolute value of the electron charge, F_π is the pion form factor and $F_j^{\mathrm{V}} = F_j^{\mathrm{p}} - F_j^{\mathrm{n}}$, $F_j^{\mathrm{S}} = F_j^{\mathrm{p}} + F_j^{\mathrm{n}}$ are the isovector and isoscalar nucleon form factors which at the photon point ($q^2 = 0$) take the values $F_1^{\mathrm{S}} = F_1^{\mathrm{V}} = 1$, $F_2^{\mathrm{S}} = \kappa^{\mathrm{p}} + \kappa^{\mathrm{n}} = -0.12$, $F_2^{\mathrm{V}} = \kappa^{\mathrm{p}} - \kappa^{\mathrm{n}} = 3.70$. We set $F_\pi = F_1^{\mathrm{V}}$ to ensure gauge invariance. It is straightforward to check gauge invariance of the amplitudes in Appendix A performing the replacement $A^\mu \to q^\mu$.

3.2. Vector mesons

The main contribution of mesons to pion photoproduction is given by ρ (isospin-1 spin-1) and ω (isospin-0 spin-1) exchange. The phenomenological Lagrangians which describe vector mesons are [9,12]

$$\mathcal{L}_\omega = -F_{\omega NN}\bar{N}\left[\gamma_\alpha - \mathrm{i}\frac{K_\omega}{2M}\gamma_{\alpha\beta}\partial^\beta\right]\omega^\alpha N + \frac{eG_{\omega\pi\gamma}}{m_\pi}\tilde{F}_{\mu\nu}(\partial^\mu\pi_j)\delta_{j3}\omega^\nu, \tag{15}$$

$$\mathcal{L}_\rho = -F_{\rho NN}\bar{N}\left[\gamma_\alpha - \mathrm{i}\frac{K_\rho}{2M}\gamma_{\alpha\beta}\partial^\beta\right]\tau_j\rho_j^\alpha N + \frac{eG_{\rho\pi\gamma}}{m_\pi}\tilde{F}_{\mu\nu}(\partial^\mu\pi_j)\rho_j^\nu. \tag{16}$$

Often the $\pi\gamma V$ coupling is written as $\mathcal{L} = \frac{eG_{V\pi\gamma}}{2m_\pi}\tilde{F}_{\mu\nu}V^{\mu\nu}\pi$ where $V^{\mu\nu} \equiv \partial^\mu V^\nu - \partial^\nu V^\mu$ and $V^\mu \equiv \rho^\mu, \omega^\mu$ [9]. Both couplings yield the same amplitude.

3.3. Spin-1/2 nucleon resonances

In the model we deal with three different kinds of resonances with spin-1/2: S_{11}, S_{31}, and P_{11}; and we need Lagrangians and amplitudes to describe their behavior. The most simple isobar is isospin-1/2 spin-1/2 (S_{11}) which can be described by the following Lagrangian

$$\mathcal{L}_{S_{11}} = -\frac{h}{f_\pi}\bar{N}\gamma_\alpha\tau_j N^*\partial^\alpha\pi_j - \frac{\mathrm{i}e}{4M}\bar{N}\gamma_{\alpha\beta}\gamma_5(g_S + g_V\tau_3)N^*F^{\alpha\beta} + \mathrm{HC}, \tag{17}$$

where HC stands for hermitian conjugate, h is the strong coupling constant which can be related to the width of the resonance decay into a nucleon and a pion, and $f_\pi = 92.3$ MeV is the leptonic decay constant of the pion. g_V and g_S stand for the resonance isovector and isoscalar form factors, respectively. They are defined as $g_V = g_p - g_n$ and $g_S = g_p + g_n$, where subscripts p and n stand for the resonances originating from the proton and the neutron, and can be related to experimental helicity amplitudes at the photon point as will be seen in the next sections. The pion coupling has been chosen pseudovector in order to obtain the right low-energy behavior and consistency with Born terms. The coupling to the photon used preserves gauge invariance.

The next isobar is isospin-3/2 spin-1/2 (S_{31}). Because of isospin we need to define isospinors as in [35]

$$N_1^* = \sqrt{\frac{1}{2}}\begin{pmatrix} N^{*++} - \sqrt{\frac{1}{3}}N^{*0} \\ \sqrt{\frac{1}{3}}N^{*+} - N^{*-} \end{pmatrix}, \tag{18}$$

$$N_2^* = \mathrm{i}\sqrt{\frac{1}{2}}\begin{pmatrix} N^{*++} + \sqrt{\frac{1}{3}} \\ \sqrt{\frac{1}{3}}N^{*+} + N^{*-} \end{pmatrix}, \tag{19}$$

$$N_3^* = -\sqrt{\frac{2}{3}}\begin{pmatrix} N^{*+} \\ N^{*0} \end{pmatrix}. \tag{20}$$

In this basis, and under the same conditions as those for previous isobar, the S_{31} Lagrangian is

$$\mathcal{L}_{S_{31}} = -\frac{h}{f_\pi}\bar{N}\gamma_\alpha N_j^*\partial^\alpha\pi_j - \frac{\mathrm{i}eg}{2M}\bar{N}\gamma_{\alpha\beta}\gamma_5 N_3^* F^{\alpha\beta} + \mathrm{HC}. \tag{21}$$

Just one electromagnetic coupling constant is needed here because only the isovector part of the photon couples to the nucleon to produce an isospin-3/2 field.

The P_{11} Lagrangian is closely related to S_{11} being parity the main change. This change is due to the angular momentum of the resonance, which implies a change in the parity of the coupling

$$\mathcal{L}_{P_{11}} = -\frac{h}{f_\pi}\bar{N}\gamma_\alpha\gamma_5\tau_j N^*\partial^\alpha\pi_j + \frac{ie}{4M}\bar{N}\gamma_{\alpha\beta}(g_S + g_V\tau_3)N^* F^{\alpha\beta} + \text{HC}. \tag{22}$$

3.4. Spin-3/2 nucleon resonances

The choice of spin-3/2 nucleon–resonance couplings is one of the main improvements of the present model compared to former ones. The choice that we use here is motivated by previous studies that identified pathologies in former spin-3/2 couplings. In what follows we provide a detailed comparison of both traditional (off-shell extension) and gauge invariant (GI) couplings, which exhibits the virtues of the choice adopted here. With regards to the traditional coupling, we restrict the discussion to the P_{33} (Δ) resonance and its coupling to the pion and the nucleon, although it affects similarly to other spin-3/2 resonances.

3.4.1. Traditional Δ–nucleon–pion coupling

The basis of the traditional point of view is the seminal paper by Nath et al. [36], based on the articles by Peccei [35] in the late sixties which dealt with this coupling. Peccei worked out a chiral Lagrangian with a pseudovector coupling to the pion, to ensure the low-energy behavior, based upon the invariance of the Δ free field under the point transformation $\Delta_\mu \to \Delta_\mu - \frac{1}{4}\gamma_\mu\gamma_\beta\Delta^\beta$ and the ansatz $\gamma^\mu O_{\mu\nu} = 0$. Given the most general Lagrangian $\mathcal{L} = h\bar{\Delta}^\mu_j O_{\mu\nu} N\partial^\nu\pi_j$ we obtain the well-known Peccei Lagrangian [35]

$$\mathcal{L}_{\text{Peccei}} = \mathrm{i}h\bar{\Delta}^\alpha_j(4g_{\alpha\beta} - \gamma_\alpha\gamma_\beta)N\partial^\beta\pi_j + \text{HC}. \tag{23}$$

Restrictions such as Peccei's ansatz are needed in order to reduce the number of degrees of freedom (DOF) of the spin-3/2 field. When a massive spin-3/2 particle is described within the Bargmann and Wigner equations [37], a problem of extra DOF arises because a vector-spinor has 16 components whilst only four are needed. These constraints naturally emerge in the free theory thanks to the Euler–Lagrange [36] or the Hamiltonian formalism [29], but for interacting particles the picture is not so straightforward and additional restrictions have to be imposed.

Nath et al. [36] proved that Peccei's ansatz was too restrictive, developing a generalization which—despite its many pathologies [29,36,38,39]—has become the traditional and most popular approach to interacting spin-3/2 particles for the last 30 years.

The starting point of Nath et al. is the massive spin-3/2 free theory, which can be found in [35,36,38]. The following Lagrangian is defined

$$\begin{aligned}\mathcal{L}_\Delta = \bar{\Delta}^\alpha\Big[&(\mathrm{i}\partial_\mu\gamma^\mu - M^*)g_{\alpha\beta} + \mathrm{i}\omega(\gamma_\alpha\partial_\beta + \gamma_\beta\partial_\alpha) + \frac{\mathrm{i}}{2}(3\omega^2 + 2\omega + 1)\gamma_\alpha\partial^\mu\gamma_\mu\gamma_\beta \\ &+ M^*(3\omega^2 + 3\omega + 1)\gamma_\alpha\gamma_\beta\Big]\Delta^\beta,\end{aligned} \tag{24}$$

where $\omega \neq -\frac{1}{2}$ and the Lagrangian is invariant under the point transformation

$$\Delta^\mu \to \Delta^\mu + a\gamma^\mu\gamma^\nu\Delta_\nu, \tag{25}$$

$$\omega \to \frac{\omega - 2a}{1 + 4a}; \tag{26}$$

with $a \neq -\frac{1}{4}$. Subsidiary constraints $\gamma_\mu \Delta^\mu = 0$ and $\partial_\mu \Delta^\mu = 0$ appear to reduce the number of DOF to four, as expected for a spin-3/2 particle. A detailed description of the DOF counting technique is given in [40]. The parameter ω does not affect physical quantities, so that one is free to set it to the most convenient value, usually $\omega = -1$ which recovers the Rarita–Schwinger theory [41].

The point transformation of Eq. (25) does not affect the spin-3/2 content of the free field because of the constraint $\gamma_\mu \Delta^\mu = 0$, but for interacting Δ particles this constraint does not apply, and the excess of DOF shows up as a contribution to the spin-1/2 sector.

The most general interacting Lagrangian containing only first-order derivatives of the pion field and consistent with (24)–(26) is given by

$$\mathcal{L}_{\text{int}} = \varkappa \bar{\Delta}^\alpha (g_{\alpha\beta} + a\gamma_\alpha \gamma_\beta) N \partial^\beta \pi + \text{HC}, \tag{27}$$

where $\varkappa$ is a coupling constant and a is called the off-shell parameter, which can be set to different values. This is named off-shell extension framework. If $a = -\frac{1}{4}$ we recover Peccei theory. This family of Lagrangians has been widely used in pion–nucleon scattering [15,42], pion photoproduction [12–17,35], and compton scattering [15,43] in the Δ-region, as well as for the description of meson exchange currents [28]. The off-shell parameter can be set to a fixed value, $a = -1$ [36], $a = -\frac{1}{4}$ [12,35] or just let it run freely [13,43] to get the best possible fit.

However, it is not possible to remove the spin-1/2 sector from the amplitude for any value of a [38]. The physical meaning of the off-shell parameter is unclear and could be considered just as a free parameter with a fuzzy physical meaning set only for fitting improvement. The disadvantage is that there is a heavy dependence of the coupling constants on the off-shell parameter, as was proved by Feuster and Mosel [13]. Other pathologies related to Eq. (27) coupling are: quantization anomalies (except for $a = -1$), so that the naive Feynman rules we *read* from the Lagrangian are no longer valid [29,36]; Johnson–Sudarshan (JS) problem (nonpositive definite commutators) [44,45] and Velo–Zwanziger (VZ) problem (acausal propagations) [45,46].

A consistent theory for interacting spin-3/2 particles is expected to be free of such problems. This theory has been developed in recent years and will be detailed in the next paragraphs.

3.4.2. Gauge invariant couplings

A different approach to massless fields of arbitrary spin λ was developed in the seventies. It was proved that the massless theory obtained from the massive one has a simple structure for both integer [47] and half-integer [48] spin fields, even if the massive theory is rather complicated. The free massless Lagrangians for half-integer spin fields can be obtained just from first principles requiring the action to be invariant under the gauge transformation $\psi \to \psi + \delta\psi$, where $\delta\psi = \partial\eta$ [49,50], ψ is a tensor-spinor with rank ℓ which stands for the particle and η a complex tensor-spinor field with rank $\ell - 1$. For a spin-3/2 field $\delta\psi_\mu = \partial_\mu \eta$, with ψ_μ a vector spinor and η a spinor field. This gauge condition reduces the number of DOF of the spin-λ field to 2—helicity states $-\lambda$ and $+\lambda$—as it is required for a massless particle. In this framework, it is quite simple to build consistent interactions for half-integer spin fields as suggested by Weinberg and Witten [51] just enforcing them to

fulfill this gauge invariance condition. For example, the spin-3/2 ψ_μ field should appear in the interaction as $\partial_\mu\psi_\nu - \partial_\nu\psi_\mu$, the spin-5/2 $\psi_{\mu\nu}$ as $\partial_\mu\partial_\nu\psi_{\rho\sigma} - \partial_\mu\partial_\sigma\psi_{\rho\sigma} - \partial_\rho\partial_\nu\psi_{\mu\sigma} + \partial_\rho\partial_\sigma\psi_{\mu\nu}$, and, more generally, an arbitrary spin-λ tensor-spinor field as the antisymmetrization of $\partial_{\alpha_1}\partial_{\alpha_2}\cdots\partial_{\alpha_{(\lambda-1/2)}}\psi_{\beta_1\beta_2\cdots\beta_{(\lambda-1/2)}}$. Thus, the vertices $\mathcal{O}^{\mu\cdots}$ of the Feynman diagrams for massless spin-3/2 particles will fulfill the condition $p_\mu\mathcal{O}^{\mu\cdots} = 0$ where p is the four momentum of the spin-3/2 particle, μ the vertex index which couples to the spin-3/2 field, and the dots stand for other possible indices. This is what is called GI coupling scheme.

We apply this procedure to the Δ case. We start from Lagrangian (24) for a free massless spin-3/2 particle. For $\omega = -1$ it can be written as

$$\mathcal{L}_{3/2,\text{massless}} = \bar{\psi}_\mu\gamma^{\mu\nu\alpha}\partial_\alpha\psi_\nu. \tag{28}$$

The inclusion of the mass term

$$\mathcal{L}_{3/2,\text{massive}} = \mathcal{L}_{3/2,\text{massless}} - M^*\bar{\psi}_\mu\gamma^{\mu\nu}\psi_\nu, \tag{29}$$

breaks gauge symmetry, raising the number of DOF from 2 to 4 as it should be.

Let us now consider the interaction. For an interacting massless spin-3/2 particle we write the Lagrangian

$$\mathcal{L} = \mathcal{L}_{3/2,\text{massive}} + \mathcal{L}_{\text{int}}. \tag{30}$$

The interaction has been built within the GI coupling scheme and can be written as [29]

$$\mathcal{L}_{\text{int}} = \psi_\mu^\dagger J^\mu + \text{HC}, \tag{31}$$

where J^μ has no dependence on ψ^μ and gauge invariance imposes $\partial_\mu J^\mu = 0$. The inclusion of the mass term—if it is properly done as in (29)—breaks gauge symmetry increasing the number of DOF of the spin-3/2 field from 2 to 4 and does not affect $\mathcal{L}_{\text{int}}$ [29,50]. Hence, the number of DOF in the interacting massive field is the right one and no unphysical components are present. Focusing on our photoproduction model, we are interested in two couplings: the Δ to the pion and the nucleon, and the Δ to the photon and the nucleon. The simplest consistent $\Delta N\pi$-coupling is [29]

$$\mathcal{L}_{\text{int}} = -\frac{h}{f_\pi M^*}\bar{N}\epsilon_{\mu\nu\lambda\beta}\gamma^\beta\gamma^5\left(\partial^\mu N_j^{*\nu}\right)(\partial^\lambda\pi_j) + \text{HC}. \tag{32}$$

We have to clarify that the vector coupling to the pion is a consequence of GI prescription. Within this prescription, the scalar coupling to the pion gives no contribution to the amplitude [29].

Concerning the $\Delta N\gamma$ coupling, Jones and Scadron's [52] suggestion has been widely used in the (G_1, G_2) decomposition with [11–14,43] or without [16,17] off-shell extension. Another decomposition (G_E, G_M), based upon the same idea as the Sachs form factors for the nucleon [53], is also possible. This decomposition is directly connected to physical quantities, as electric and magnetic multipoles, in particular to the E2/M1 ratio which is of great interest from both experimental and theoretical points of view [6,19,24]. This second decomposition is consistent with the GI approach and can be written as [54]

$$\mathcal{L} = \frac{3e}{2M(M+M^*)}\bar{N}\left[\text{i}g_1\tilde{F}_{\mu\nu} + g_2\gamma^5F_{\mu\nu}\right]\left(\partial^\mu N_3^{*\nu}\right) + \text{HC}, \tag{33}$$

where g_1 and g_2 can be easily related to G_E and G_M [40] by

$$G_{\mathrm{E}} = -\frac{1}{2}\frac{M^* - M}{M^* + M} g_2, \tag{34}$$

$$G_{\mathrm{M}} = g_1 + \frac{1}{2}\frac{M^* - M}{M^* + M} g_2. \tag{35}$$

Other possible consistent choices can be found in [40,55].

GI couplings have been proved to be free of the pathologies which are inherent to the traditional scheme. No anomalies are found in the quantization; neither JS nor VZ problems appear; and no spin-1/2 sector arises when the invariant amplitudes are calculated [29]. Moreover, Pascalutsa and Timmermans [40] claim that DOF counting is the reason why GI couplings are consistent while the off-shell extension couplings of Nath et al. are not. They blame the unphysical extra components for the appearance of pathologies. Both, GI (32) and traditional (27) couplings, provide the same result on-shell (if we set properly the coupling constants). However, their off-shell behavior is completely different.

Based on the previous discussion, the P_{33} Lagrangian that will be used in this work is

$$\begin{aligned}\mathcal{L}_{\mathrm{P}_{33}} = &-\frac{h}{f_\pi M^*}\bar{N}\epsilon_{\mu\nu\lambda\beta}\gamma^\beta\gamma^5\left(\partial^\mu N_j^{*\nu}\right)(\partial^\lambda \pi_j) \\ &+\frac{3e}{2M(M+M^*)}\bar{N}\left[\mathrm{i}g_1\tilde{F}_{\mu\nu} + g_2\gamma^5 F_{\mu\nu}\right]\left(\partial^\mu N_3^{*\nu}\right) + \mathrm{HC}.\end{aligned} \tag{36}$$

From this Lagrangian it is straightforward to obtain phenomenological Lagrangians for other spin-3/2 resonances. To obtain the P_{13} resonance Lagrangian from (36) only an isospin change is needed

$$N_j^{*\alpha} \to \tau_j N^{*\alpha}, \quad j = 1, 2, 3; \tag{37}$$

for the strong vertex, and

$$N_3^{*\alpha} \to N^{*\alpha}, \quad g_j \to \tfrac{1}{2}\left[g_j^{\mathrm{S}} + g_j^{\mathrm{V}}\tau_3\right], \quad j = 1, 2; \tag{38}$$

for the photon vertex.

Thus, the Lagrangian is

$$\begin{aligned}\mathcal{L}_{\mathrm{P}_{13}} = &-\frac{h}{f_\pi M^*}\bar{N}\epsilon_{\mu\nu\lambda\beta}\gamma^\beta\gamma^5\tau_j(\partial^\mu N^{*\nu})(\partial^\lambda \pi_j) \\ &+\frac{3e}{4M(M+M^*)}\bar{N}\left[\mathrm{i}\left(g_1^{\mathrm{S}} + g_1^{\mathrm{V}}\tau_3\right)\tilde{F}_{\mu\nu} + \left(g_2^{\mathrm{S}} + g_2^{\mathrm{V}}\tau_3\right)\gamma^5 F_{\mu\nu}\right](\partial^\mu N^{*\nu}) + \mathrm{HC}.\end{aligned} \tag{39}$$

Lagrangians for D_{33} and D_{13} resonances are obtained easily from P_{33} and P_{13}. We only need to change the parity of the coupling placing an overall γ_5

$$\begin{aligned}\mathcal{L}_{\mathrm{D}_{33}} = &-\frac{h}{f_\pi M^*}\bar{N}\epsilon_{\mu\nu\lambda\beta}\gamma^\beta\left(\partial^\mu N_j^{*\nu}\right)\left(\partial^\lambda \pi_j\right) \\ &+\frac{3e}{2M(M+M^*)}\bar{N}\left[\mathrm{i}g_1\tilde{F}_{\mu\nu}\gamma_5 + g_2 F_{\mu\nu}\right]\left(\partial^\mu N_3^{*\nu}\right) + \mathrm{HC},\end{aligned} \tag{40}$$

$$\mathcal{L}_{\mathrm{D}_{13}} = -\frac{h}{f_\pi M^*}\bar{N}\epsilon_{\mu\nu\lambda\beta}\gamma^\beta\tau_j(\partial^\mu N^{*\nu})(\partial^\lambda\pi_j) + \frac{3e}{4M(M+M^*)}\bar{N}\left[\mathrm{i}\left(g_1^{\mathrm{S}}+g_1^{\mathrm{V}}\tau_3\right)\tilde{F}_{\mu\nu}\gamma_5 + \left(g_2^{\mathrm{S}}+g_2^{\mathrm{V}}\tau_3\right)F_{\mu\nu}\right](\partial^\mu N^{*\nu}) + \mathrm{HC}. \tag{41}$$

Although we restrict ourselves to spin-3/2, it is clear that higher spin interactions can be built within the same theoretical framework. This is left to future works.

3.5. Propagators and widths

With regards to the propagators of the resonances, for a spin-1/2 resonance we use

$$\mathrm{i}G(v) = \mathrm{i}\frac{\not{v}+M^*}{v^2-M^{*2}+\mathrm{i}M^*\Gamma(s,u)}, \tag{42}$$

and for the spin-3/2 propagator we use the Rarita–Schwinger propagator

$$\mathrm{i}G_{\alpha\beta}(v) = \mathrm{i}\frac{\not{v}+M^*}{v^2-M^{*2}+\mathrm{i}M^*\Gamma(s,u)}\left[-g_{\alpha\beta}+\frac{1}{3}\gamma_\alpha\gamma_\beta+\frac{2}{3M^{*2}}v_\alpha v_\beta-\frac{1}{3M^*}\left(v_\alpha\gamma_\beta-\gamma_\alpha v_\beta\right)\right], \tag{43}$$

where v is the resonance four momentum. A phenomenological width $\Gamma(s,u)$ is included in the propagator denominator consistently with what is obtained if we dress it with pions [54,56].

The energy dependence of the width is chosen phenomenologically as

$$\Gamma(s,u) = \sum_j \Gamma_j X_j(s,u), \tag{44}$$

where $j = \pi, \pi\pi, \eta$ stands for the different decay channels and

$$X_j(s,u) \equiv X_j(s) + X_j(u) - X_j(s)X_j(u), \tag{45}$$

with $X_j(l)$ given by

$$X_j(l) = 2\frac{\left(|\vec{k}_j|\big/|\vec{k}_{j0}|\right)^{2L+1}}{1+\left(|\vec{k}_j|\big/|\vec{k}_{j0}|\right)^{2L+3}}\Theta\left(l-(M+m_j)^2\right), \tag{46}$$

where L is the angular momentum of the resonance, Θ is the Heaviside step function, and

$$|\vec{k}_j| = \sqrt{\left(l-M^2-m_j^2\right)^2-4m_j^2M^2}\Big/\left(2\sqrt{l}\right), \tag{47}$$

with $m_{\pi\pi} \equiv 2m_\pi$ and $|\vec{k}_{j0}| = |\vec{k}_j|$ when $l = M^{*2}$.

This parametrization has been built in order to fulfill the following conditions:

(i) $\Gamma = \Gamma_0$ at $\sqrt{s} = M^*$,
(ii) $\Gamma \to 0$ when $|\vec{k}_j| \to 0$,
(iii) a correct angular momentum barrier at threshold $|\vec{k}_j|^{2L+1}$,
(iv) crossing symmetry.

This parametrization of the width is an improvement over the one used in [12] and includes decays to η and 2π which take into account inelastic channels [9] and condition (iv). The width contributes to both s and u-channels, so that crossing symmetry is preserved due to Eq. (45). In [13], the authors made an analysis of the energy dependence of the width. It was concluded that, as long as it provides a decrease of the width beyond the resonance position, the specific way in which X_j is parametrized is not so important.

3.6. Form factors

For the numerical calculations we include form factors for Born terms and vector mesons, to regularize the high-energy behavior of these terms. We choose form factors as suggested by Davidson and Workman [57] that allow to fulfill gauge invariance and crossing symmetry. Actually, $X_j(s,u)$ in Eq. (45) also follows this choice. Thus, for Born terms

$$\hat{F}_{\mathrm{B}}(s,u,t) = F_1(s) + F_2(u) + F_3(t) - F_1(s)F_2(u) - F_1(s)F_3(t) - F_2(u)F_3(t) + F_1(s)F_2(u)F_3(t), \tag{48}$$

where

$$F_1(s) = \left[1 + \left(s - M^2\right)^2/\Lambda_{\mathrm{B}}^4\right]^{-1}, \tag{49}$$

$$F_2(u) = \left[1 + \left(u - M^2\right)^2/\Lambda_{\mathrm{B}}^4\right]^{-1}, \tag{50}$$

$$F_3(t) = \left[1 + \left(t - m_\pi^2\right)^2/\Lambda_{\mathrm{B}}^4\right]^{-1}. \tag{51}$$

For vector mesons we adopt $\hat{F}_{\mathrm{V}}(t) = F_3(t)$ with the changes $m_\pi \to m_{\mathrm{V}}$ and $\Lambda_{\mathrm{B}} \to \Lambda_{\mathrm{V}}$. In order to have as few free parameters as possible in the numerical calculations we use the same $\Lambda \equiv \Lambda_{\mathrm{B}} = \Lambda_{\mathrm{V}}$ for both vector mesons and Born terms. For the resonance–pion–nucleon vertex, the form factor $\sqrt{X_\pi(s,u)}$ has to be used for consistency with the width used in the propagator discussed previously.

Models like the ones by Garcilazo and Moya de Guerra [12] and Feuster and Mosel [13] needed a cutoff in the u-channels of spin-3/2 resonances to obtain a good description of observables. This cutoff was needed because the high-energy contributions of these diagrams are not reduced by the denominator of the propagator. In [12], it was argued that the need of this cutoff could be justified by the two possible interpretations of the resonance excitation. From an effective field theory point of view, u-channels should be introduced with their full strength. On the other hand, if we consider resonances as pure πN rescattering states (Chew–Low description), the u-channel contributions should be dropped. Hence, the cutoff was interpreted in [12] as a way to have an interplay between both descriptions. However, in this way crossing symmetry was broken. Our present model relies entirely on effective field theory, and we preserve crossing symmetry and there is no need for that cutoff in the u-channel amplitudes. Ought to the vector coupling to the resonance the u-channel amplitudes are suppressed by themselves which is a strong point in favor of the GI coupling.

4. Results

4.1. Study of the parameters of the model

The first choice that has to be made is the nucleon resonances to be taken into account. We have included seven resonances: $\Delta(1232)$, $N(1440)$, $N(1520)$, $N(1535)$, $\Delta(1620)$, $N(1650)$, and $\Delta(1700)$ which are all the four star nucleon resonances in PDG up to 1.7 GeV and up to spin-3/2. Among four star resonances only spin-5/2 N(1675) and N(1680) resonances are left aside for future work.

In a Lagrangian model, the determination of the parameters of a single resonance is affected by the determination of the parameters of the other resonances. Thus, we have decided not to include three star resonances because their contribution would be very small and would introduce a sort of noise in the determination of the parameters.

There are quite a number of parameters to be set in the model. Some of them are well known and established independently of the photoproduction data, such as nucleon and pion masses ($M = 938.9175$ MeV, $m_{\pi^0} = 134.9766$ MeV, $m_{\pi^\pm} = 139.5673$ MeV), but some others have to be established from fits to the pion photoproduction data, namely electromagnetic coupling constants. In the forthcoming paragraphs, we give the values of every parameter of the model as well as the procedures employed to establish them.

4.1.1. Vector meson coupling constants

Vector meson contributions are characterized by 11 parameters: m_ω, $F_{\omega NN}$, K_ω, $G_{\omega\pi\gamma}$, m_{ρ^0}, $m_{\rho^\pm}$, $F_{\rho NN}$, K_ρ, $G_{\rho^0\pi\gamma}$, $G_{\rho^\pm\pi\gamma}$, and cutoff Λ. Masses are given by PDG and the $\pi\gamma V$ couplings are related to the decay widths $\Gamma_{\pi\gamma V}$ of PDG [30] through the equation

$$\Gamma_{V\to\pi\gamma} = \frac{e^2 G_{V\pi\gamma}^2}{96\pi}\frac{m_V^3}{m_\pi^2}\left(1-\frac{m_\pi^2}{m_V^2}\right)^3. \tag{52}$$

We take from PDG the following values: $m_\omega = 782.57$ MeV, $m_{\rho^0} = 768.5$ MeV, $m_{\rho^\pm} = 766.5$ MeV, $\Gamma_{\rho^0\pi\gamma} = 0.121$ MeV ($G_{\rho^0\pi\gamma} = 0.1161$), $\Gamma_{\rho^\pm\pi\gamma} = 0.068$ MeV ($G_{\rho^\pm\pi\gamma} = 0.0906$), and $\Gamma_{\omega\pi\gamma} = 0.70476$ MeV ($G_{\omega\pi\gamma} = 0.2804$). Thus, only five constants remain unknown. One of them is the cutoff Λ which will be discussed later. The four remaining constants are taken from the analysis of nucleon electromagnetic form factors by Mergell et al. [58]: $F_{\rho NN} = 2.6$, $K_\rho = 6.1 \pm 0.2$, $F_{\omega NN} = 20.86 \pm 0.25$, and $K_\omega = -0.16 \pm 0.01$, which compare well to the data, including the latest experiments at Jefferson Lab [59].

4.1.2. Masses and widths of the nucleon resonances

We have used three different sets of masses and widths of the nucleon resonances (Table 1): First, the PDG values [30]; second, the multichannel analysis of Vrana et al. [60]; and third, the speed plot (SP) calculation that we explain below. For the partial decay widths we have two different sets, one from PDG and one from Vrana et al. which lies within the PDG error bars. The Vrana et al. set of partial decay widths has been chosen for the SP calculation.

Masses and widths of nucleon resonances can be obtained from πN partial wave analysis using the speed plot technique [61]. First, we define the speed by

$$SP(W) = |\mathrm{d}T(W)/\mathrm{d}W|, \tag{53}$$

Table 1
Masses, widths, and branching ratios from [30,60] and from the speed plot calculation (see text)

	$\Delta(1232)$	$N(1440)$	$N(1520)$	$N(1535)$	$\Delta(1620)$	$N(1650)$	$\Delta(1700)$
M^*_{P}	1210	1365	1510	1505	1607	1660	1660
M^*_{V}	1217	1383	1504	1525	1607	1663	1726
M^*_{SP}	1211	1372	1516	1540	1608	1664	1641
Γ_{P}	100	210	115	170	115	160	200
Γ_{V}	96	316	112	102	148	240	118
Γ_{SP}	98	290	48	107	141	159	955
$\frac{\Gamma_\pi}{\Gamma_{\mathrm{P}}}$	1.00	0.65	0.55	0.45	0.25	0.72	0.15
$\frac{\Gamma_\eta}{\Gamma_{\mathrm{P}}}$	—	0.00	0.00	0.51	—	0.06	—
$\frac{\Gamma_{\pi\pi}}{\Gamma_{\mathrm{P}}}$	0.00	0.35	0.45	0.04	0.75	0.22	0.85
$\frac{\Gamma_\pi}{\Gamma_{\mathrm{V}}}$	1.00	0.72	0.63	0.35	0.45	0.74	0.05
$\frac{\Gamma_\eta}{\Gamma_{\mathrm{V}}}$	—	0.00	0.00	0.51	—	0.06	—
$\frac{\Gamma_{\pi\pi}}{\Gamma_{\mathrm{V}}}$	0.00	0.28	0.37	0.14	0.55	0.20	0.95

Masses and widths in MeV. We have taken $\Gamma_{\pi\pi}/\Gamma = 1 - \Gamma_\pi/\Gamma - \Gamma_\eta/\Gamma$. Subscripts P, V, and SP stand for PDG [30], Vrana [60], and Speed Plot, respectively. PDG masses and widths are mean values.

with $W = \sqrt{s}$ and

$$T(W) = \frac{1}{2\mathrm{i}}\left[\exp(2\mathrm{i}\delta(W)) - 1\right], \tag{54}$$

where $T(W)$ is the dimensionless resonance partial wave amplitude and $\delta(W)$ its phase.

To calculate masses and widths we have taken phases from the current solution of the SAID πN partial wave analysis [4]. In Fig. 3 we show $SP(W)$ for P_{33}—in the $\Delta(1232)$ region—and S_{11} multipoles. The position of the peak provides the pole mass, and the height provides the width: $H = 2/\Gamma$.

The baryon resonances show up clearly and the calculation is straightforward. The only problem is related to the existence of a background which induces a phase shift in the πN phases. In the region of the peak this phase shift can be considered approximately constant and its effect in $SP(W)$ is negligible.

Our fits to photoproduction data shown in the next subsections are classified according to six sets of parameters which are given in Table 2. Sets #1 and #4 are based on PDG values for masses and widths; set #2 and set #4 are based on Vrana et al. [60]; and sets #3 and #6 are based on the SP calculation.

The strong coupling constants (h's) of the resonances are obtained from equations in Appendix B, using the partial decay widths into one pion of the resonances. We choose all the strong coupling constants to be positive, thus the overall sign of the amplitude of each resonance depends on the sign of the electromagnetic coupling constants.

4.1.3. Electromagnetic coupling constants of the nucleon resonances

At this point, only the electromagnetic coupling constants and the cutoff Λ remain undetermined. The best way to establish them is by fitting to pion photoproduction experimental data. Among all the observables (cross-section, asymmetries, etc.) for pion photoproduction, the set of data we have chosen is the one given by the current SAID multipole energy-independent solution [2–4]. There are two main reasons for this choice. First, electromagnetic multipoles are directly related to the amplitudes and are more sensitive to

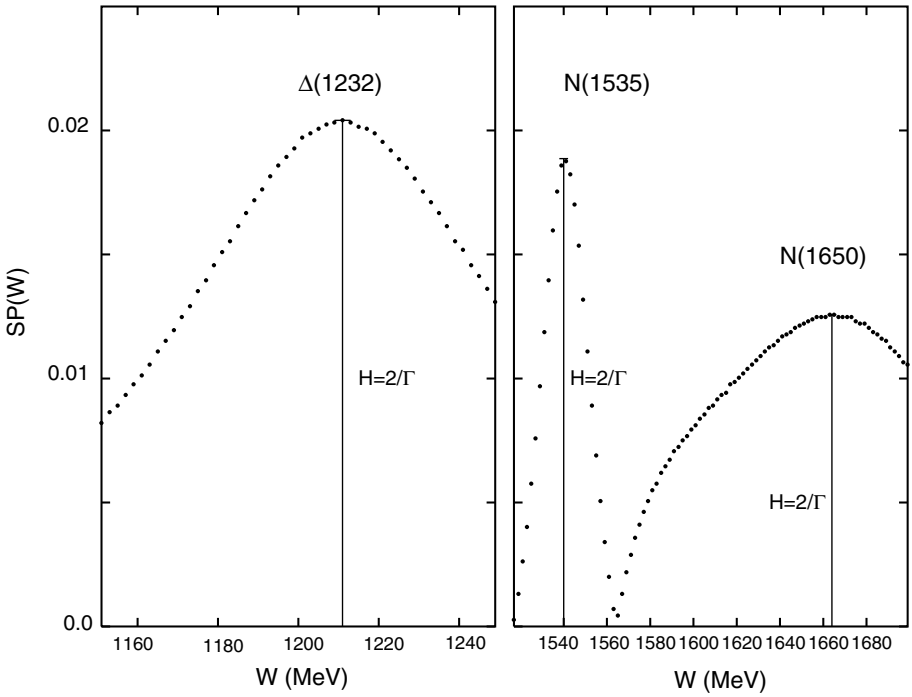

Fig. 3. Speed plot examples. Left figure shows the $\Delta(1232)$ speed plot. Right figure shows the speed plot for the S_{11} region. Data have been taken from SAID database for πN scattering [4].

coupling properties than are other observables. Deficiencies in the model show up much more clearly in multipoles than in any other observable. Second, all the observables can be expressed in terms of the multipoles, thus, if the multipoles are properly fitted by the model, so should be the other observables. The explicit expressions for the multipoles in terms of the amplitudes can be found in Appendix C.

Another issue to take into account is unitarity. Models below the two pion production threshold fulfill Watson's theorem [62] to achieve unitarity using either πN scattering phases [9], dynamical models [16–19] or K-matrix [11]. Beyond the two pion production limit, implementation of unitarity is unclear and usually relies on experimental data and/or extensions of the methods applied below the two pion threshold.

We would like to note that, although our calculation seems to be at tree-level, it is not quite so due to the inclusion of the width and the form factors, which take into account higher-order diagrams and structure effects. If we perform a truly tree-level calculation—straightforwardly from amplitudes of Appendix A—we would find out that all the amplitudes are real and that it would be impossible to fulfill the unitarity condition $SS^\dagger = 1$, where S is the scattering matrix. In an effective Lagrangian perturbative model, unitarity should be restored by the inclusion of higher-order diagrams. To avoid this tedious and difficult task, we adopt a phenomenological point of view. The main higher-order effects can be taken into account including a width in the propagator, as we do in Section 3.5 (which amounts to dress the propagator), and including also effective final state interactions (FSI). Once the width is included, unitarity restoration may be achieved

Table 2
Specifications of the parameter sets

Set	#1	#2	#3	#4	#5	#6
Masses and widths	PDG	Vrana	SP	PDG	Vrana	SP
δ_{FSI}	Yes	Yes	Yes	No	No	No
$\chi^2/\chi^2_{\mathrm{PDG}}$	1	0.53	0.60	9.30	5.57	4.56
Λ	1.121	1.050	1.040	1.494	0.951	0.962
K_ρ	6.30	6.30	6.30	6.30	5.90	5.90
$F_{\omega NN}$	21.11	21.11	21.11	20.61	21.11	21.11
K_ω	−0.17	−0.17	−0.17	−0.15	−0.17	−0.17
$M^*[\Delta(1232)]$	1.209	1.215	1.209	1.210	1.215	1.209
$\Gamma[\Delta(1232)]$	0.102	0.098	0.100	0.102	0.094	0.099
$M^*[N(1440)]$	1.385	1.381	1.370	1.385	1.381	1.370
$\Gamma[N(1440)]$	0.160	0.318	0.292	0.260	0.314	0.288
$M^*[N(1520)]$	1.505	1.502	1.514	1.505	1.502	1.514
$\Gamma[N(1520)]$	0.110	0.110	0.050	0.110	0.110	0.050
$M^*[N(1535)]$	1.495	1.527	1.542	1.495	1.523	1.538
$\Gamma[N(1535)]$	0.250	0.104	0.109	0.099	0.100	0.109
$M^*[\Delta(1620)]$	1.590	1.605	1.606	1.620	1.605	1.606
$\Gamma[\Delta(1620)]$	0.100	0.150	0.143	0.100	0.150	0.143
$M^*[N(1650)]$	1.680	1.665	1.666	1.640	1.665	1.666
$\Gamma[N(1650)]$	0.150	0.238	0.157	0.150	0.242	0.157
$M^*[\Delta(1700)]$	1.620	1.728	1.639	1.620	1.728	1.639
$\Gamma[\Delta(1700)]$	0.250	0.120	0.957	0.250	0.120	0.957

Masses, widths, and Λ are in GeV. The coupling constants for the vector mesons are dimensionless. We provide also the $\chi^2/\chi^2_{\mathrm{PDG}}$ to compare fits.

through FSI. We can assume that it is possible to isolate the FSI effects factorizing the multipoles $\mathcal{M}$ in the following way:

$$\mathcal{M}^{I,\ell,\Pi} = \left|\mathcal{M}^{I,\ell,\Pi}\right| \exp[\delta_{\mathrm{width}}] F^{I,\ell,\Pi}, \tag{55}$$

where $F^{I,\,\ell,\Pi}$ is a phase factor that takes into account FSI, and ℓ stands for orbital angular momentum, Π for parity, and I for isospin:

$$F^{I,\ell,\Pi} = \exp\left[\mathrm{i}\delta^{I,\ell,\Pi}_{\mathrm{FSI}}\right]. \tag{56}$$

Then, the absolute value of the multipoles must be well reproduced by the model and only the phases of the multipoles remain unknown. We are interested in the bare values of the coupling constants, so the best choice is to use directly the experimental phases. Hence, the multipole phase can be written as

$$\delta^{I,\ell,\Pi} = \delta_{\mathrm{width}} + \delta^{I,\ell,\Pi}_{\mathrm{FSI}}, \tag{57}$$

where we call δ_{width} to the phase given by the calculated amplitudes and comparison with experimental phase shifts ($\delta^{I,\ell,\Pi}$) provides us with the unknown final state interaction phase shifts $\delta^{I,\ell,\Pi}_{\mathrm{FSI}}$. Phases $\delta^{I,\ell,\Pi}$ are taken from the current energy-dependent multipole solution of SAID analysis [2–4]. For each set of masses and widths we obtain two types of fits, one with and one without SAID phases.

To fit the data and determine the best parameters of the resonances we have written a genetic algorithm combined with the E04FCF routine from NAG libraries [63]. Although genetic algorithms are computationally more expensive than other algorithms, in a minimization problem it is much less likely for them to get stuck at local minima than for other methods, namely gradient-based minimization methods. Thus, in a multiparameter minimization like the one we face here it is probably the best possibility to search for the minimum. It is out of the scope of this paper to go through an explanation on genetic algorithms and details on them can be found elsewhere [64].

The function to minimize the χ^2 is defined as

$$\chi^2 = \sum_j \frac{\left(\mathcal{M}_j^{\text{exp}} - \mathcal{M}_j^{\text{th}}\right)^2}{\left(\Delta\mathcal{M}_j^{\text{exp}}\right)^2}, \tag{58}$$

where $\mathcal{M}^{\text{exp}}$ stands for the current energy-independent extraction of the multipole analysis of SAID up to 1 GeV for E_{0+}, M_{1-}, E_{1+}, M_{1+}, E_{2-}, and M_{2-} multipoles in the three isospin channels $I = \frac{3}{2}, p, n$ for the $\gamma p \to \pi^0 p$ process. $\Delta\mathcal{M}^{\text{exp}}$ is the error and $\mathcal{M}^{\text{th}}$ is the multipole given by the model which depends on the parameters. These parameters are the cutoff Λ and the electromagnetic coupling constants in Table 3, which are related to the helicity amplitudes A_λ^I in Table 4 through equations given in Appendix D.

The minimization procedure applied is as follows: First, the genetic algorithm has been run and when the convergence conditions were accomplished the E04FCF routine was used for fine tuning. The program has been run many times with different seeds to ensure that the minimum was not local. We have taken into account 763 data for the real part of the multipoles and the same amount for the imaginary part. Thus, 1526 data points have been used in the fits.

In Tables 2–4 we show results for the six different sets and provide the reader with all the parameters of the model. Table 2 shows masses and widths, the cutoff Λ, as well as the vector meson parameters K_ρ, $F_{\omega NN}$, and K_ω, for each set. Table 3 provides all the coupling constants of the resonances as well as the the E2/M1 Ratio (EMR) of the $\Delta(1232)$ resonance. Table 4 contains the helicity amplitudes of the resonances which can be compared to those in other references such as [11–13,30].

4.2. Multipole analysis

As has been previously explained, in order to determine the parameters of the resonances and the cutoff we have used the data for electromagnetic multipoles. In this section, we discuss the results obtained for multipoles as well as the quality of the different fits.

Lagrangian models like the one presented here are more complicated than Breit–Wigner models such as MAID [9]. The latter are simple and describe accurately experimental observables but do not provide much information about properties of the resonances such as the strength of the couplings. Breit–Wigner treatment of resonances can be considered naive because each resonance contributes only to the multipole with its same angular momentum quantum number. In this way, there is no background from resonances, which is very different from Lagrangian models where, for a given resonance, the direct term contributes only to a single spin–isospin channel, while the crossed term contributes to different spin–isospin channels as background, and then one resonance does indeed affect the

Table 3
Coupling constants of the resonances

			#1	#2	#3	#4	#5	#6
$\Delta(1232)$	P_{33}	h	0.764	0.721	0.757	0.759	0.706	0.753
		g_1	6.061	5.574	5.630	6.254	5.382	4.984
		g_2	2.414	1.187	1.123	4.032	7.253	7.696
		G_E	−0.152	−0.076	−0.071	−0.255	−0.466	−0.485
		G_M	6.213	5.650	5.701	6.509	5.848	5.469
		EMR	−2.45%	−1.35%	−1.24%	−3.92%	−7.97%	−8.87%
$N(1440)$	P_{11}	h	0.213	0.304	0.303	0.272	0.302	0.300
		g^p	0.255	−0.269	−0.247	0.255	−0.164	0.017
		g^n	−0.125	0.273	0.234	−0.125	0.096	−0.128
$N(1520)$	D_{13}	h	0.560	0.567	0.366	0.560	0.567	0.360
		g_1^p	−5.753	−4.848	−5.607	−5.498	−0.580	−2.348
		g_1^n	1.217	2.829	1.982	0.301	−1.503	0.105
		g_2^p	−0.861	−0.645	−0.520	−0.920	−0.986	−0.691
		g_2^n	1.462	0.960	0.979	1.674	2.731	2.174
$N(1535)$	S_{11}	h	0.132	0.079	0.078	0.083	0.078	0.079
		g^p	0.219	0.078	0.028	0.435	0.230	0.084
		g^n	−0.102	−0.127	−0.080	−0.164	−0.195	−0.129
$\Delta(1620)$	S_{31}	h	0.133	0.159	0.155	0.126	0.159	0.155
		g	−0.154	−0.324	−0.308	−0.063	0.008	0.044
$N(1650)$	S_{11}	h	0.102	0.132	0.107	0.110	0.134	0.107
		g^p	0.113	−0.167	0.025	0.117	0.074	0.127
		g^n	0.018	0.411	0.324	0.019	0.281	0.056
$\Delta(1700)$	D_{33}	h	0.285	0.149	0.528	0.285	0.149	0.528
		g_1	−3.513	0.663	−11.875	−3.996	−19.642	−26.531
		g_2	1.871	0.548	−2.392	2.000	3.701	7.293

The E2/M1 ratio (EMR) of $\Delta(1232)$ is also given. All magnitudes are dimensionless.

determination of the parameters of other resonances. Contributions from crossed terms to the background cannot be neglected and there are resonant contributions to several multipoles. For instance, $N(1520)$ contributes to $E_{2-}^{p,n}$ and $M_{2-}^{p,n}$, as expected for a D_{13} isobar, but also contributes strongly to M_{1+}^{p}. Thus, the background of Breit–Wigner models is much simpler because it only has contributions from Born terms and vector mesons (ρ and ω).

Figs. 4–6 show the comparison of the six different sets of Table 2 to experimental data from SAID database [4]. Without FSI, at low energies, we get nice fits to some of the multipoles: $M_{1+}^{3/2}$, $E_{2-}^{3/2}$, and E_{2-}^{p}. With increasing energy there is a breakdown of the model which calls for further improvements. The major ingredient that lacks the model is FSI, which we introduce phenomenologically as described in Section 4.1.3. Indeed, the fits are greatly improved—specially the fits of the imaginary parts of the multipoles—when FSI are included, as it stems from the comparison of the χ^2 (Table 2). The experimental data are quite well reproduced by theory with better quality for the low-energy region than for the high energy (900 MeV and further), where some of the fits start to diverge (i.e., $\mathrm{Im}M_{1+}^{p}$ and $\mathrm{Im}E_{0+}^{n}$). In this section, we focus on fits that include FSI, except in the case in which comparison with nonFSI sets provides relevant information.

Table 4
Helicity amplitudes in $\mathrm{GeV}^{-1/2}$ for the different sets

			#1	#2	#3	#4	#5	#6
$\Delta(1232)$	P_{33}	$A^{\Delta}_{1/2}$	−0.129	−0.123	−0.123	−0.129	−0.101	−0.090
		$A^{\Delta}_{3/2}$	−0.247	−0.225	−0.224	−0.263	−0.248	−0.231
$N(1440)$	P_{11}	$A^{p}_{1/2}$	−0.061	0.064	0.058	−0.061	0.039	−0.004
		$A^{n}_{1/2}$	0.030	−0.065	−0.055	0.030	−0.023	0.030
$N(1520)$	D_{13}	$A^{p}_{1/2}$	−0.020	−0.020	−0.034	−0.015	0.027	0.006
		$A^{n}_{1/2}$	−0.050	−0.013	−0.022	−0.068	−0. 121	−0.092
		$A^{p}_{3/2}$	0.161	0.129	0.136	0.161	0.095	0.092
		$A^{n}_{3/2}$	−0.128	−0.118	−0.107	−0.128	−0. 190	−0.163
$N(1535)$	S_{11}	$A^{p}_{1/2}$	0.060	0.022	0.008	0.119	0.065	0.024
		$A^{n}_{1/2}$	−0.028	−0.036	−0.023	−0.045	−0. 055	−0.037
$\Delta(1620)$	S_{31}	$A^{\Delta}_{1/2}$	0.038	0.081	0.077	0.016	−0.002	−0.011
$N(1650)$	S_{11}	$A^{p}_{1/2}$	0.037	−0.054	0.008	0.037	0.024	0.041
		$A^{n}_{1/2}$	0.006	0.133	0.105	0.006	0.091	0.018
$\Delta(1700)$	D_{33}	$A^{\Delta}_{1/2}$	0.109	0.015	0.222	0.119	0.406	0.573
		$A^{\Delta}_{3/2}$	0.063	0.055	0.057	0.063	−0.156	0.006

Despite the difference between SP and Vrana et al.'s masses and widths, the curves that we obtain for sets #2 and #3 are very close to each other (so are their χ^2, see Table 2), sometimes undistinguishable, except for some high-order multipoles as $\mathrm{Im}M^{p}_{2-}$. Curves from set #1 do not reproduce data as well as #2 and #3 do and the χ^2 is almost twice as large due to the additional restrictions in the values of the parameters.

If we go through the multipoles in detail, it is convenient to start with $E^{3/2}_{1+}$ and $M^{3/2}_{1+}$ (both in Fig. 4) which provide information about the most important low-lying nucleon resonance, the $\Delta(1232)$. These multipoles are of great interest at present and a lot of experimental effort has been put in the study of the $\Delta(1232)$ in the last years [6,65]. The $M^{3/2}_{1+}$ presents a quite simple structure which is very well reproduced by all our sets and it is not affected by FSI. That is why all sets are quite similar. Sets #1, #4, and #5 overestimate the multipole peaks which will cause an overestimation of the cross-section as will be seen in Section 4.5. The situation is much more complicated for the $E^{3/2}_{1+}$, where the FSI are critical, as can be inferred when we compare data to sets with and without FSI and check the strong differences among them. For these multipoles, data cannot be reproduced well without the inclusion of δ_{FSI}. When the latter is included the multipoles show a discontinuity at $\sqrt{s} = 1.249$ GeV due to an abrupt change in SAID phases at that energy.

An important quantity related to $\Delta(1232)$ is the E2/M1 Ratio (EMR) which is related to the deformation of the nucleon [6,19,24]. This quantity can be defined as the $G_{\mathrm{E}}/G_{\mathrm{M}}$ ratio

$$\mathrm{EMR} = \frac{G_{\mathrm{E}}}{G_{\mathrm{M}}} = -\frac{(M_{\Delta} - M)g_2}{2(M_{\Delta} + M)g_1 + (M_{\Delta} - M)g_2} \times 100\%. \tag{59}$$

We obtain a negative value for this ratio, which according to [14] corresponds to an oblate deformation. The values from the most reliable fits (sets #2 and #3) are very similar, around −1.3%. This result compares well to some other analysis: −1.45% (K-matrix) [11]; −1.42% (ELA) [12]; −1.43% (ELA) [14]; −2.7% (dynamical model) [17]; −2.09% (dynamical model) [18]. However, it is quite different from the result recently obtained

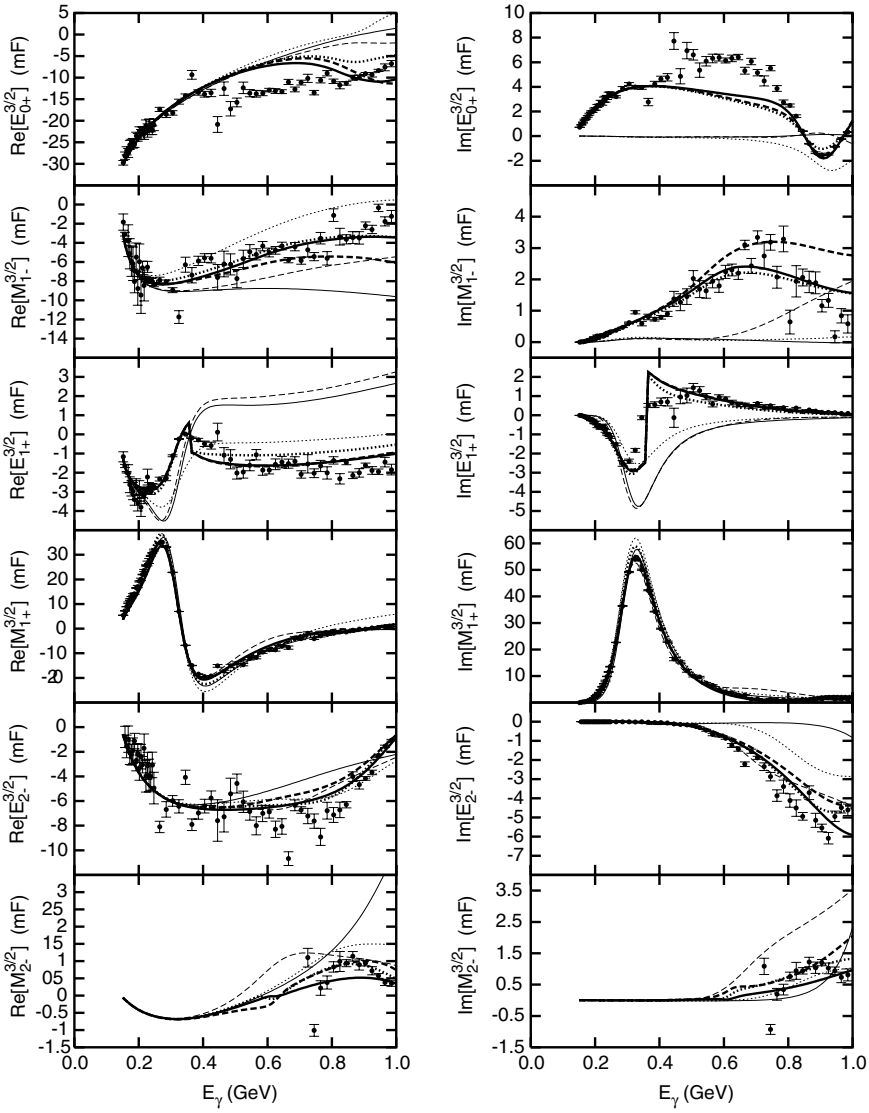

Fig. 4. Electromagnetic multipoles for the isospin-3/2 channel. Data have been taken from [4]. Photon energy is given in the laboratory frame. Curves conventions: thick dotted set #1; thick solid set #2; thick dashed set #3; thin dotted set #4; thin solid set #5; thin dashed set #6.

by Pascalutsa and Tjon (EMR = 3.8%) [19] within a dynamical model. This ratio is discussed in more detail in [66].

The multipoles M_{1-}^{p} and M_{1-}^{n} are closely related to the $N(1440)$ resonance. If we focus on sets #2 and #3, when δ_{FSI} is included the fits look quite well except for the real part of the M_{1-}^{n} (second figure of the left panel in Fig. 6) where a serious discrepancy between theory and data is found in the 0.2–0.5 GeV energy range. Also, a rather odd behavior in the M_{1-}^{p} is found between 0.3 and 0.4 GeV (see Fig. 5), where no experimental data are available. For these multipoles related to $N(1440)$ resonance, background and resonant

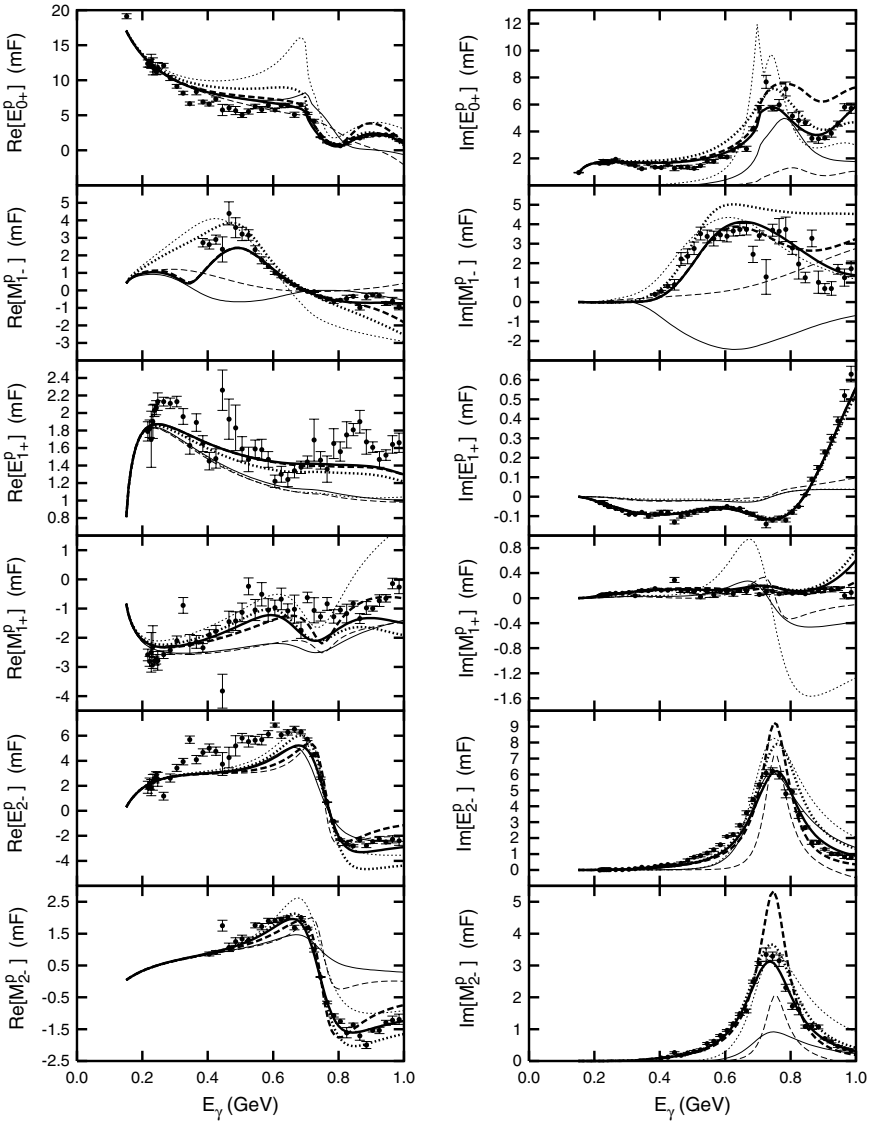

Fig. 5. Electromagnetic multipoles for the isospin-1/2 proton channel. Same conventions as in Fig. 4 apply. Data have been taken from [4].

contributions are not well established. As a consequence, the parameters of the P_{11} resonance cannot be well determined. These multipoles also show the importance of FSI in the model in order to determine the properties of the resonances because of the large discrepancies among fits with and without δ_{FSI}. However, if we focus on sets #1 and #4, FSI do not seem so important if the PDG values are used. Actually, set #4 provides better results than set #1 except for the high-energy region of $\mathrm{Re}\,M^{\mathrm{p}}_{1-}$ and $\mathrm{Re}\,M^{\mathrm{n}}_{1-}$. More research on the properties of this resonance (and of its role in nuclear medium) has to be done in forthcoming years [1].

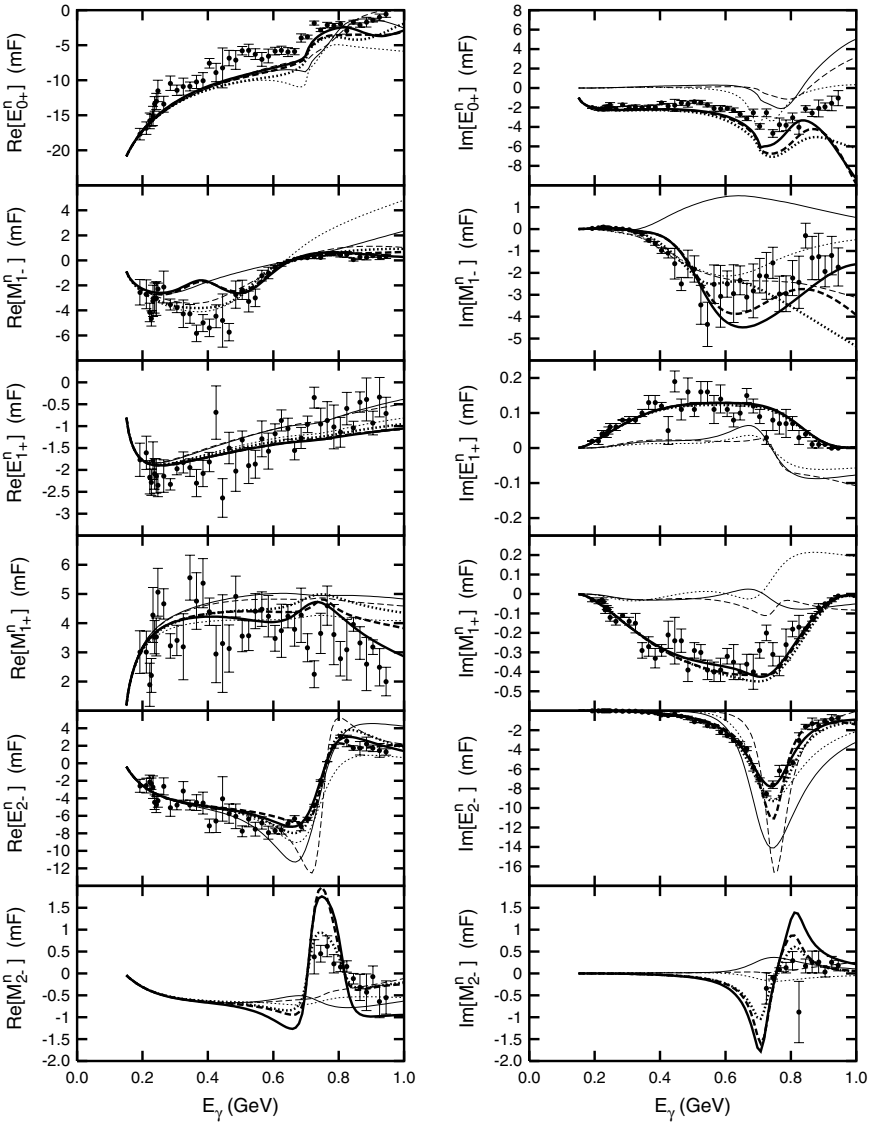

Fig. 6. Electromagnetic multipoles for the isospin-1/2 neutron channel. Same conventions as in Fig. 4 apply. Data have been taken from [4].

Resonance $N(1520)$ contributes mainly to $E_{2-}^{\mathrm{p,n}}$ and $M_{2-}^{\mathrm{p,n}}$ due to its angular momentum and isospin. It also contributes sizeably to other multipoles. The s-channel contributes to M_{1+}^{p} and its crossed term to $\mathrm{Im}M_{1-}^{3/2}$ as background. It also has small contributions to the background of other multipoles. Considering set #2 and multipoles $E_{2-}^{\mathrm{p,n}}$ and $M_{2-}^{\mathrm{p,n}}$, the agreement is excellent except where there are few experimental data. Set #3 overestimates the peak of the resonance in the multipoles and so will do for the cross-section.

$E_{0+}^{3/2,\mathrm{p,n}}$ multipoles get contributions from Born terms and vector mesons mainly. Resonances $N(1535)$, $\Delta(1620)$, and $N(1650)$ only contribute in the high-energy region, but in that region they acquire great importance defining the shape of the multipoles. For example, the cusp peak that shows up in $\mathrm{Im}\,E_{0+}^{\mathrm{p,n}}$ (Figs. 5 and 6) is due to the structure of the phenomenological width—Eq. (44)—and to the inclusion of the partial decay width Γ_η/Γ in $N(1535)$ resonance. Multipoles $E_{0+}^{\mathrm{p,n}}$ are well reproduced by sets #2 and #3, except in the high-energy region of $\mathrm{Im}\,E_{0+}^{\mathrm{n}}$. The multipole $E_{0+}^{3/2}$ (Fig. 4) is not so well reproduced in the intermediate energy region (0.4–0.8 GeV), with an overestimation of the real part and an underestimation of the imaginary part. This indicates that the prediction of the model is correct for the absolute values of the multipoles and that there may be a problem with the phases.

Only one resonance remains, $\Delta(1700)$, which is associated mainly to multipoles $E_{2-}^{3/2}$ and $M_{2-}^{3/2}$. As one can see in Fig. 4, when enough data points are available the fits are good, yet the large ambiguities in the mass and width of this resonance make somewhat unreliable the determination of its coupling constants and its contribution to the observables (see Table 3). Further research on the properties of this resonance is necessary.

In Fig. 7, we show two examples of the various contributions to the multipoles using the coupling constants of set #2. It is clear that, without FSI, the Born terms and vector mesons do not contribute to the imaginary part of the multipoles and represent a background—it has to be noticed that when the FSI are included, they do contribute to both real and imaginary parts of the multipole. Left panel shows the multipole $M_{1+}^{3/2}$, whose main contribution is the $\Delta(1232)$. In this multipole, FSI are not important and curves with and without SAID phases differ little. Thus, the phenomenological width included is enough to describe accurately the multipole and its structure is quite simple.

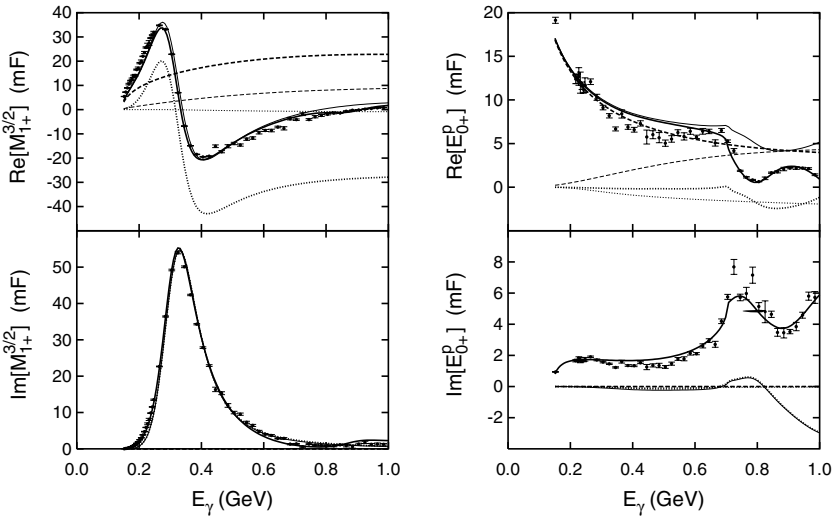

Fig. 7. Examples of various contributions to the multipoles. Left panel shows the $M_{1+}^{3/2}$ multipole, right panel the E_{0+}^{p} multipole. Data have been taken from [4]. All the curves have been obtained using set #2 parameters. Thick dashed: Born terms contribution; thin dashed: vector meson contributions; thick dotted: direct terms contribution from resonances; thin dotted: crossed terms contribution from resonances; thin solid: full calculation without FSI; thick solid: full calculation with FSI.

However, the situation is different for the multipole E_{0+}^{p} which presents a more complex structure because its dominant contribution comes from Born terms and vector mesons. In the absence of FSI, the imaginary part of this multipole is practically zero up to 0.8 GeV. While inclusion of FSI makes Born and vector mesons contribute to the imaginary part too, improving agreement with data.

We have not considered spin-5/2 resonances in the model. This will be required in order to extend the model to multipoles of higher angular momentum. For the energy range considered here, their contribution is expected not to be important, although their contribution to the background could improve the agreement with data.

4.3. Results at threshold energy

Special attention has to be paid to the behavior of the model at low/threshold energy, because cross-sections and multipoles are well predicted by low-energy theorems (LET) [67] and chiral perturbation theory (ChPT) [22,23]. Owing to the change in the spin-3/2 coupling scheme, the threshold energy results change substantially when compared to previous works. In particular, in [12], using the off-shell formalism, it was found that the contributions from resonances, direct and crossed terms, were of great importance to explain the reduced cross-section at threshold and the low-energy behavior of the cross-section. These contributions were specially important in neutral processes, mainly because of $\Delta(1232)$, and were almost the total contribution to the $n\pi^0$ production channel [68]. However, in the present calculation we obtain a zero contribution to the reduced cross-section at threshold from both direct and crossed resonance terms. The reason for such a change is the spin-3/2 coupling scheme used in the present article, which has no spurious spin-1/2 sector. The reduced differential cross-section at threshold is proportional to the E_{0+} multipole [23] which is a spin-1/2 multipole. Thus, at threshold, any contribution of the direct channel from spin-3/2 resonances is a contamination which unveils a pathology in the model. This is the case of models based upon the traditional spin-3/2 formalism explained in Section 3.4.1, as the one used in [12]. This result is independent on the phenomenology of the decay width and on the form factors. Therefore, we conclude that, at threshold, only Born terms (Fig. 1) and vector mesons (Fig. 2E) contribute, as the spin-1/2 resonances are at much higher energy. In Table 5, we present results for the reduced cross-section at threshold for the four different processes and we find a good agreement with experimental values. Tiny differences are found with various parameter sets (#1–#6) that use different cutoff Λ and small variations in the vector meson parameters.

Table 5
Reduced cross-section at threshold $\frac{q^*}{k^*}\frac{d\sigma}{d\Omega}$ in μb/sr

Sets	#1	#2	#3	#4	#5	#6	Experiment
$\gamma p \to p\pi^0$	0.0984	0.0998	0.0998	0.0949	0.1023	0.1020	0.094 ± 0.017
$\gamma n \to n\pi^0$	0.0046	0.0045	0.0045	0.0049	0.0044	0.0044	
$\gamma n \to p\pi^-$	18.92	18.93	18.93	18.91	18.95	18.95	20.4 ± 0.7
							20.0 ± 0.3
							19.7 ± 1.4
$\gamma p \to n\pi^+$	14.51	14.50	14.50	14.52	14.48	14.49	15.4 ± 0.5
							15.6 ± 0.5

Experimental data have been taken from [12].

4.4. Differential cross-sections and asymmetries

In this section, we show results for the differential cross-sections together with results for five asymmetries: the recoil nucleon polarization, P; the polarized target asymmetry, T; the polarized beam asymmetry, Σ; and the double polarization parameters G and H. Details on the definition of these quantities can be found in [8,34,69]. The asymmetries are of great interest in the search of *missing* resonances which do not show up so clearly in other observables [70]. The formulae which relate the amplitudes with the asymmetries will be presented in forthcoming paragraphs. We provide the reader with a wide sample of figures to have a broad outlook of the model compared to data whenever available.

The FSI treatment described in Section 4.1.3 has been applied only to the $\gamma p \to \pi^0 p$ process. For the other three pion production processes, no FSI phases have been included because we have no means to determine them from the data available. We calculate the observables for these processes for the six sets of coupling constants obtained by fitting $\gamma p \to \pi^0 p$ multipoles, given in Tables 2 and 3. Thus, these calculations have no adjustable parameters. As we shall see in what follows an overall good agreement with data has been found. As the energy increases, differences among the curves obtained with the different sets of parameters show up more data favoring the sets of coupling constants obtained using FSI.

4.4.1. $\gamma p \to \pi^0 p$

Let us first consider the process $\gamma p \to \pi^0 p$, for which the experimental database has been largely increased in the last 10 years mainly thanks to the experimental programs developed at Mainz (MAMI) and Brookhaven (LEGS). For this process, the amount of experimental information is much larger than for any other pion photoproduction process. Even so, the database on asymmetries is not yet large enough and more measurements are needed to fill in the existing gaps. Figs. 8 and 9 show theoretical curves for the differential cross-sections compared to experimental data. Differential cross-sections have been calculated using equations from Section 2 and amplitudes from Appendix A.

Because of parity, among the eight helicity amplitudes, only four of them are independent

$$H_1 = \mathcal{A}_{1/2,-1/2,1} = -\mathcal{A}_{-1/2,1/2,-1}, \tag{60}$$

$$H_2 = \mathcal{A}_{-1/2,-1/2,1} = \mathcal{A}_{1/2,1/2,-1}, \tag{61}$$

$$H_3 = \mathcal{A}_{1/2,1/2,1} = \mathcal{A}_{-1/2,-1/2,-1}, \tag{62}$$

$$H_4 = \mathcal{A}_{-1/2,1/2,1} = -\mathcal{A}_{1/2,-1/2,-1}. \tag{63}$$

In terms of these four independent helicity amplitudes (see Section 2 for $\mathcal{A}_{\lambda_1,\lambda_2,\lambda_\gamma}$ definition), it is possible to define all the physical observables [2]. In particular, the five asymmetries previously mentioned.

Focusing on sets with δ_{FSI} phases, the fits are qualitatively good in the whole energy region, and even quantitatively so in the range 250–400 MeV. Asymmetries are well predicted in almost the whole energy range.

In Fig. 10, we provide recoil nucleon polarization asymmetries (P) defined by

$$\sigma(\theta)P = -\frac{1}{64\pi^2 s^*}\frac{k^*}{E_\gamma^*}\mathrm{Im}\,[H_2\bar{H}_4 + H_1\bar{H}_3], \tag{64}$$

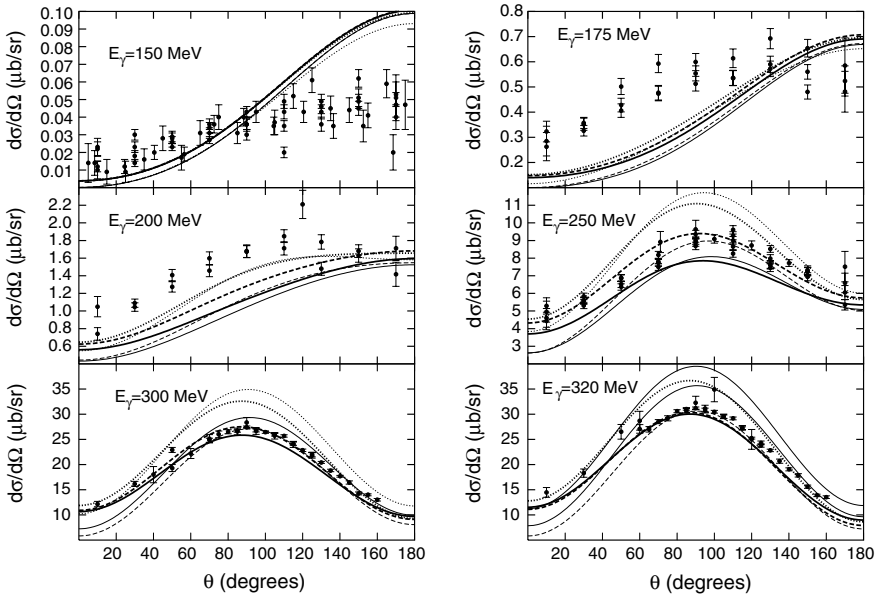

Fig. 8. Differential cross-section in μb/sr of the $\gamma p \to \pi^0 p$ reaction for different photon energies in the laboratory frame. Pion scattering angle θ in the center of mass reference system. Experimental data have been taken from [4] and are within the range $E_\gamma \pm 1$ MeV. Curve conventions: thick dotted set #1; thick solid set #2; thick dashed set #3; thin dotted set #4; thin solid set #5; thin dashed set #6.

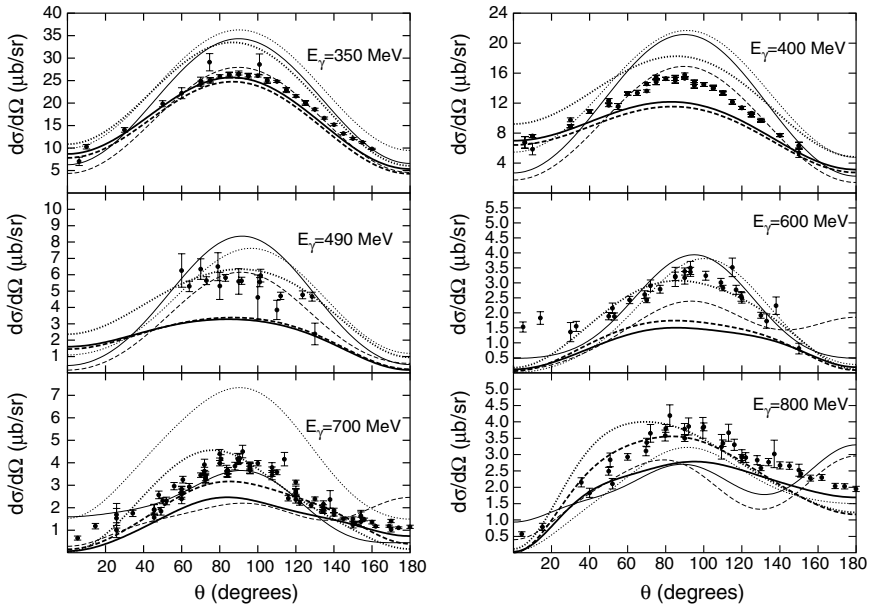

Fig. 9. Same as in Fig. 8. Experimental data are within the range $E_\gamma \pm 3$ MeV.

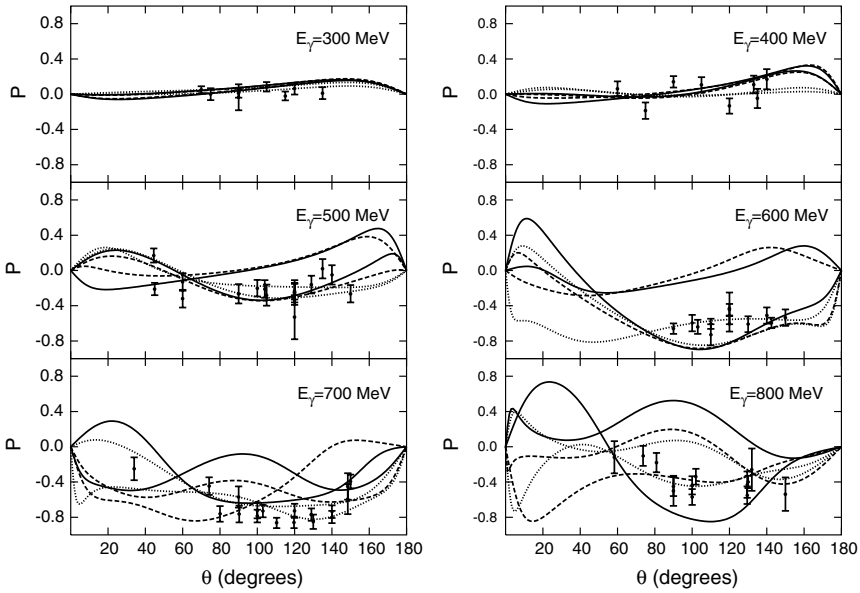

Fig. 10. Recoil nucleon polarization of the $\gamma p \to \pi^0 p$. Photon energy in the laboratory frame. Pion angle in the center of mass reference system. Experimental data are within the range $E_\gamma \pm 3$ MeV. Conventions for the curves are as in Fig. 8.

where the bar over the helicity amplitudes H_j stands for complex conjugate and $\sigma(\theta)$ for the differential cross-section given by Eq. (5). Up to 600 MeV, data are well reproduced by sets with FSI. Above this energy, data are reproduced qualitatively but not quantitatively.

In Fig. 11, we present polarized target asymmetry (T) given by equation

$$\sigma(\theta)T = \frac{1}{64\pi^2 s^*}\frac{k^*}{E_\gamma^*}\mathrm{Im}\,[H_2\bar{H}_1 + H_4\bar{H}_3]. \tag{65}$$

Up to 400 MeV the six curves are very similar. For 500 and 580 MeV, the sets with phases provide good results and the sets without phases do not. The high-energy region (700 and 800 MeV) is not well reproduced in general.

Polarized beam asymmetry (Σ) is well predicted in the whole energy range by sets with FSI (Fig. 12). Even sets without FSI provide good results except in the very high energy region (800 MeV). Helicity amplitudes are related to Σ through

$$\sigma(\theta)\Sigma = \frac{1}{64\pi^2 s^*}\frac{k^*}{E_\gamma^*}\mathrm{Re}\,[H_2\bar{H}_3 - H_1\bar{H}_4]. \tag{66}$$

In short, compared to data, good agreement is obtained for energies below 800 MeV. Beyond that energy some observables (e.g., Σ) are also reasonably well described.

In the energy region considered here there are no experimental data on the other two asymmetries G and H. These asymmetries are expressed in terms of helicity amplitudes by means of the following equations:

$$\sigma(\theta)G = -\frac{1}{64\pi^2 s^*}\frac{k^*}{E_\gamma^*}\mathrm{Im}\,[H_2\bar{H}_3 + H_1\bar{H}_4], \tag{67}$$

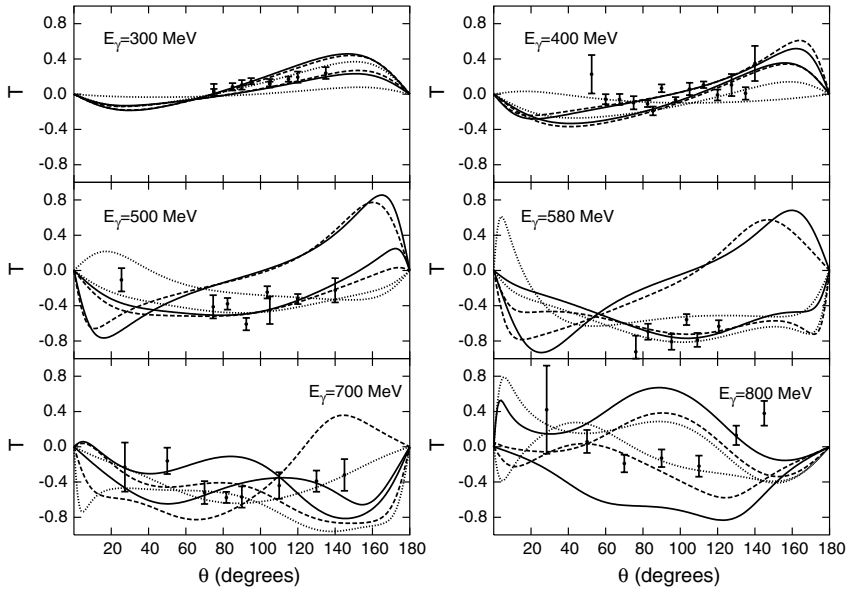

Fig. 11. Polarized target asymmetry of the $\gamma p \to \pi^0 p$ reaction. Experimental data are within the range $E_\gamma \pm 3$ MeV. Same conventions as in Fig. 10.

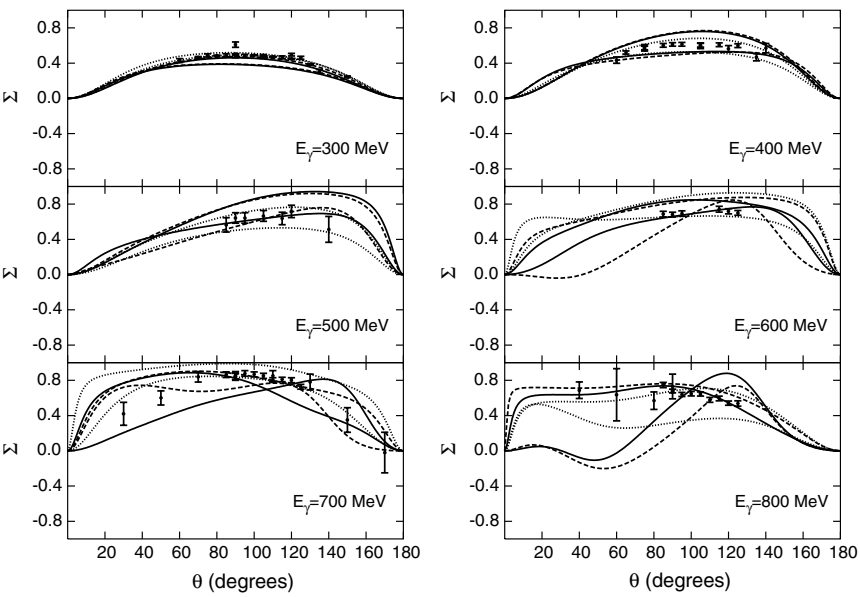

Fig. 12. Photon beam asymmetry of the $\gamma p \to \pi^0 p$ reaction. Experimental data are within the range $E_\gamma \pm 3$ MeV. Same conventions as in Fig. 10.

$$\sigma(\theta)H = -\frac{1}{64\pi^2 s^*}\frac{k^*}{E_\gamma^*}\mathrm{Im}\,[H_2\bar{H}_4 + H_3\bar{H}_1]. \tag{68}$$

We have also calculated these asymmetries and our results are presented in Figs. 13 and 14.

4.4.2. $\gamma n \to \pi^0 n$

The situation for the $\gamma n \to \pi^0 n$ process is quite different from the previous case. The amount of experimental information is very small: No asymmetry data are available and the differential cross-section data are scant. In Fig. 15, we show differential cross-sections and in Figs. 16–20 the predicted asymmetries (P, T, Σ, G, and H, respectively) obtained with sets of parameters. There is a reasonable agreement with data, and sets #1 and #4 (PDG values) provide the best results globally.

4.4.3. Charged pion production

In the next paragraphs we go in detail through the predicted differential cross-sections and asymmetries for charged pion processes, and compare them to available data (Figs. 21–32).

$\gamma p \to \pi^+ n$ differential cross-sections (Fig. 21) are well predicted by the model in the whole energy range by all parameter sets. In the high-energy regime (two last figures of the panels) differential cross-sections are not well predicted by any of the parameter sets in the forward scattering region, with the exception of set #1 (PDG with δ_{FSI}) which provides an impressively good agreement. For the P asymmetry (Fig. 22) all curves are alike and reproduce data correctly up to 400 MeV. As the energy is increased, sets #1 and #4 (PDG values) provide the best results. The T asymmetry is qualitatively well predicted, but quantitative agreement is only achieved up to 500 MeV (Fig. 23). Sets with and without FSI provide a good agreement with data for the Σ asymmetry (Fig. 24). Only in the last figure of the panel (700 MeV) we observe different qualitative behaviors from one set of constants to another. Data

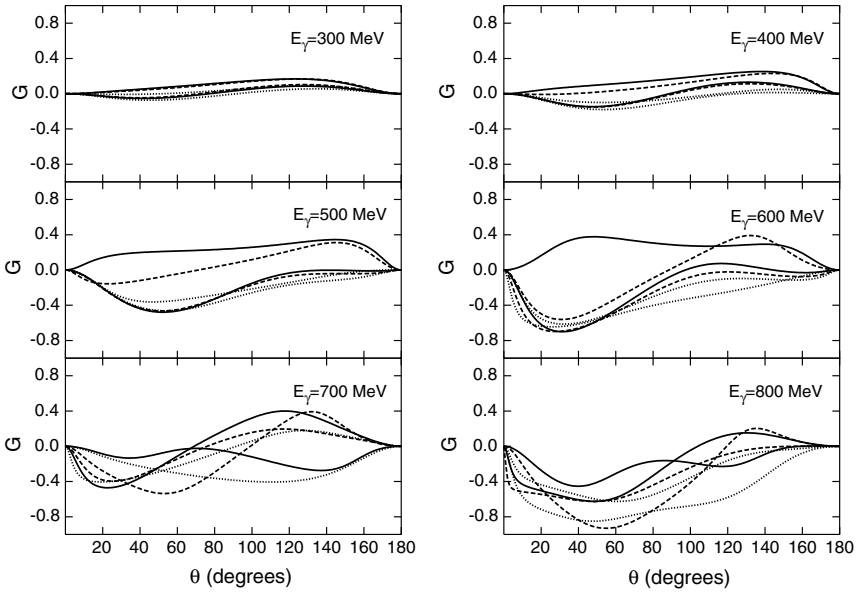

Fig. 13. G asymmetry of the $\gamma p \to \pi^0 p$ reaction. Same conventions as in Fig. 10.

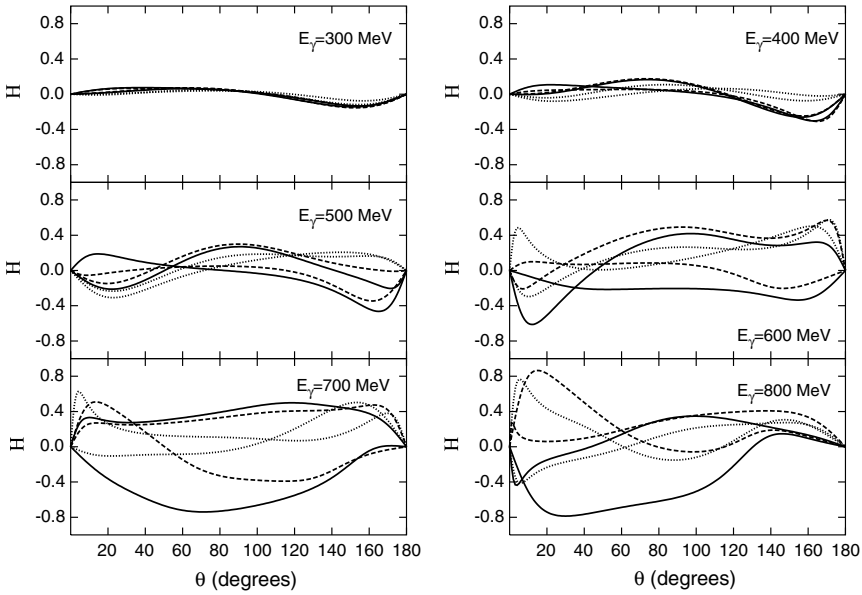

Fig. 14. H asymmetry of the $\gamma p \to \pi^0 p$ reaction. Same conventions as in Fig. 10.

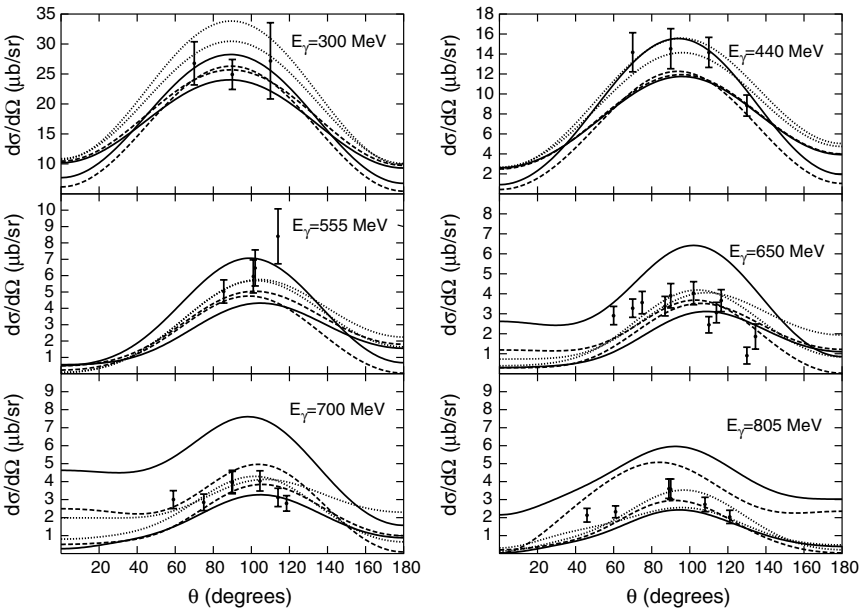

Fig. 15. Differential cross-section of the $\gamma n \to \pi^0 n$ reaction. Experimental data are within the range $E_\gamma \pm 5$ MeV. Same conventions as in Fig. 8.

are scant and not reliable for G and H asymmetries. As in previous asymmetries, in the low-energy regime all the curves are alike, but as energy is increased their predictions become quite different.

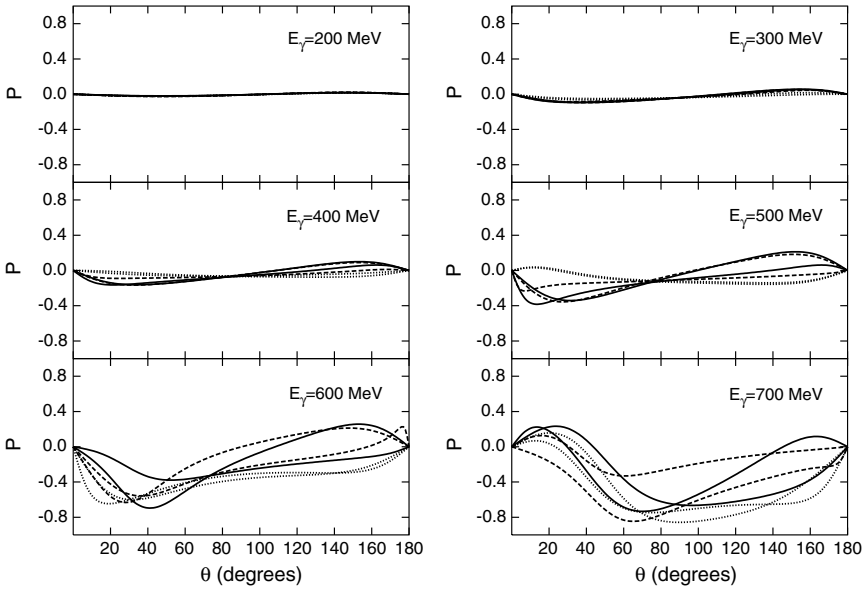

Fig. 16. Recoil nucleon polarization of the $\gamma n \to \pi^0 n$. Same conventions as in Fig. 10.

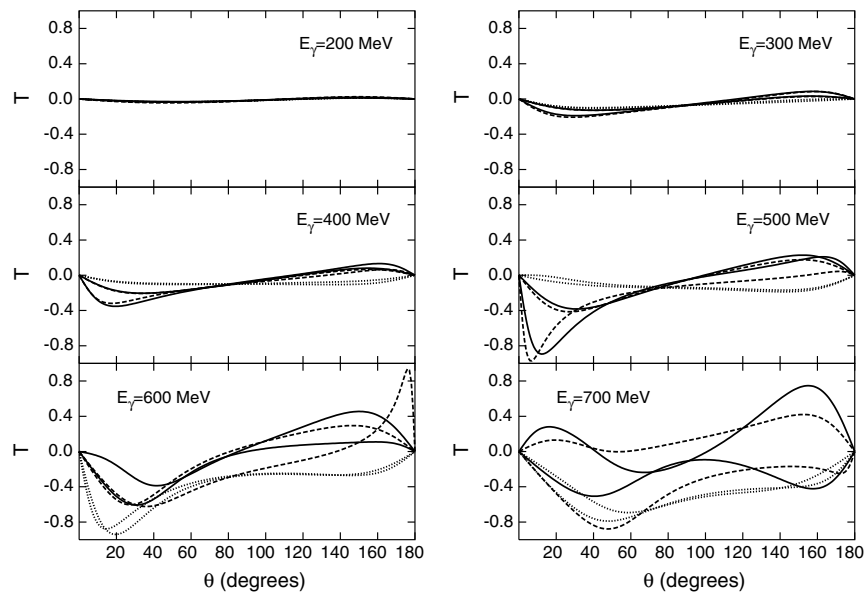

Fig. 17. Polarized target asymmetry of the $\gamma n \to \pi^0 n$ reaction. Same conventions as in Fig. 10.

Differential cross-section data for the reaction $\gamma p \to \pi^- p$ are well predicted by the sets with FSI (#1, #2, and #3). All the curves are similar for the P asymmetry (Fig. 28) and are close to data. Overall agreement is good for the T asymmetry (Fig. 29). This agreement becomes excellent for the highest energy ($E_\gamma = 802$ MeV) if

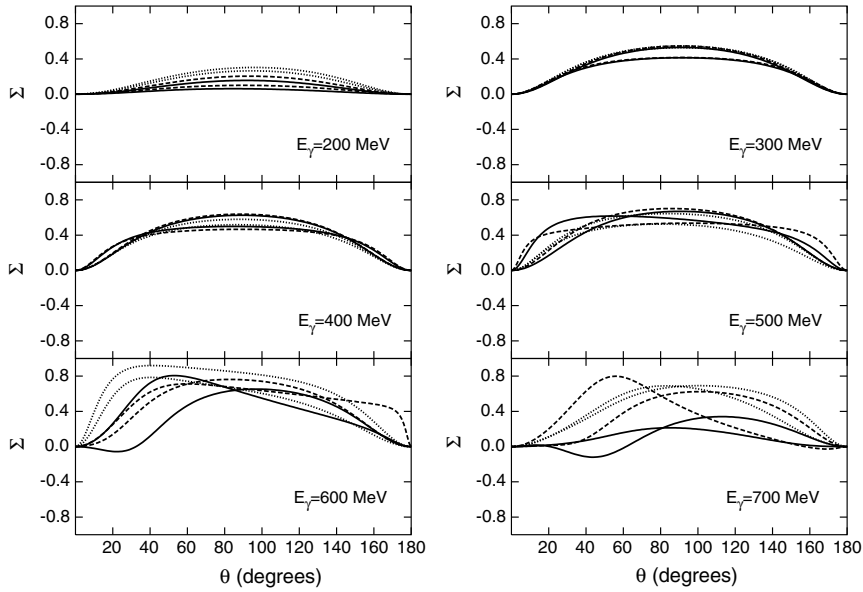

Fig. 18. Photon beam asymmetry of the $\gamma n \to \pi^0 n$ reaction. Same conventions as in Fig. 10.

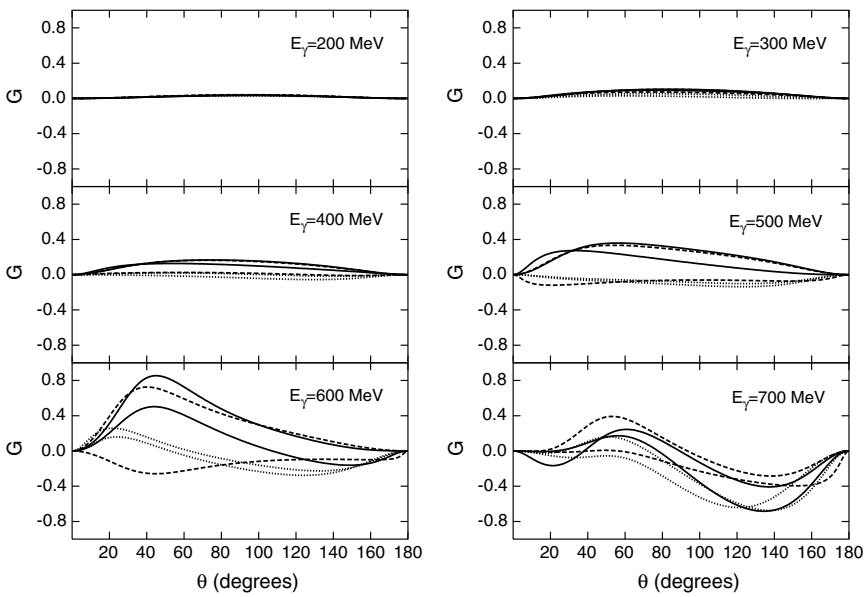

Fig. 19. G asymmetry of the $\gamma n \to \pi^0 n$ reaction. Same conventions as in Fig. 10.

we consider only curves #2 and #3. Σ asymmetry (Fig. 30) is very well predicted by curves #2 and #3 in the whole energy range. All predictions are qualitatively quite similar for the G and H asymmetries (Figs. 31 and 32) except for $E_\gamma = 800$ MeV, where large differences are found.

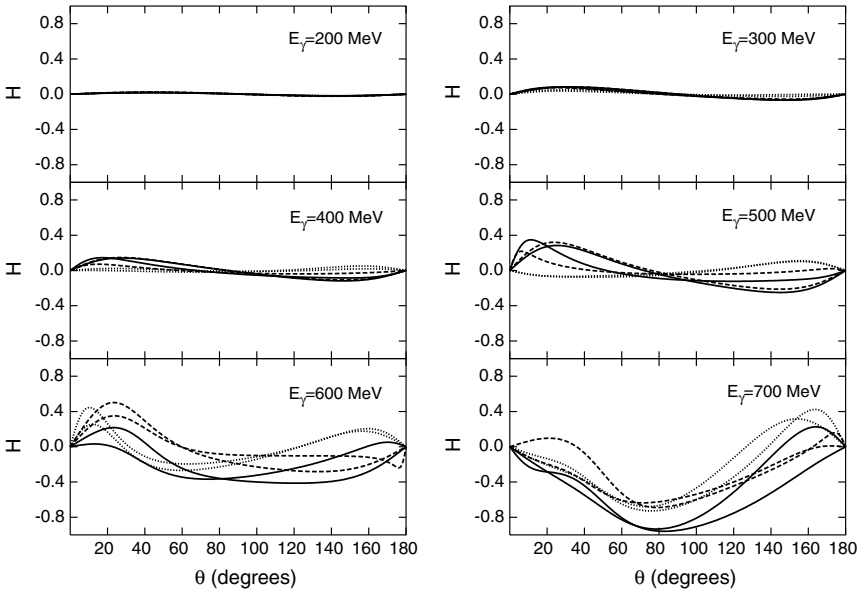

Fig. 20. H asymmetry of the $\gamma n \to \pi^0 n$ reaction. Same conventions as in Fig. 10.

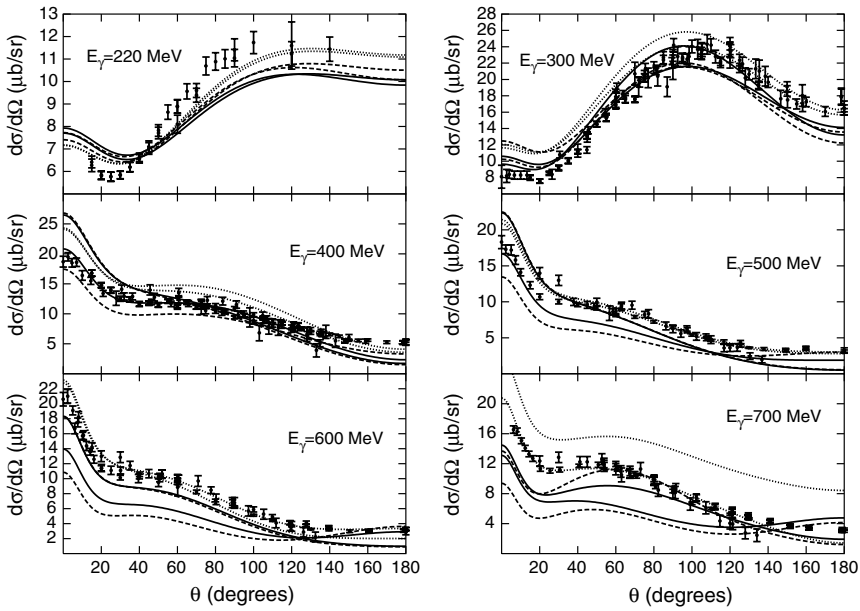

Fig. 21. Differential cross-section of the $\gamma p \to \pi^+ n$ reaction. Experimental data are within the range $E_\gamma \pm 5$ MeV. Same conventions as in Fig. 8.

The model works quite well for processes with charged pion. So, this is remarkable if we take into account that no δ_{FSI} have been included, and indicates that FSI are not as important in the studied energy region, for charged pions as they are for neutral pion channels.

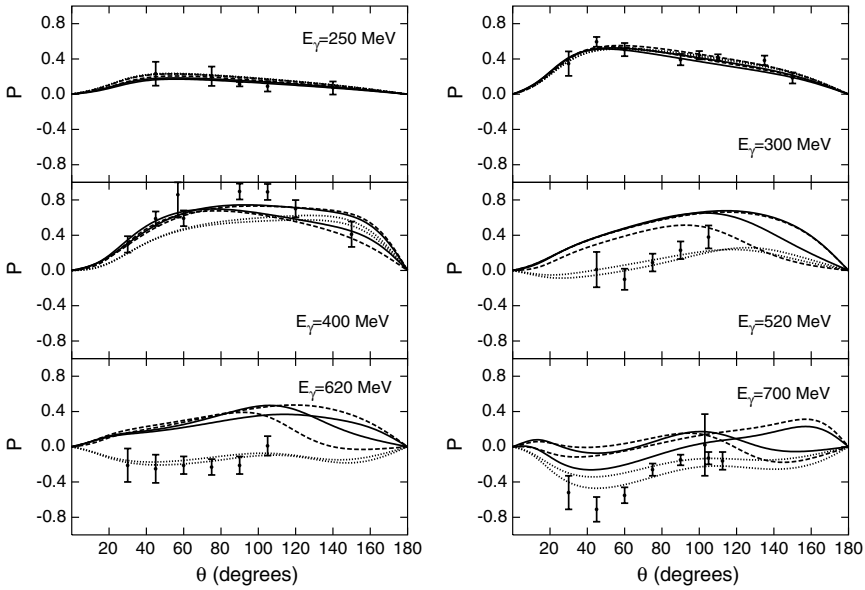

Fig. 22. Recoil nucleon polarization of the $\gamma p \to \pi^+ n$ reaction. Experimental data are within the range $E_\gamma \pm 3$ MeV. Same conventions as in Fig. 10.

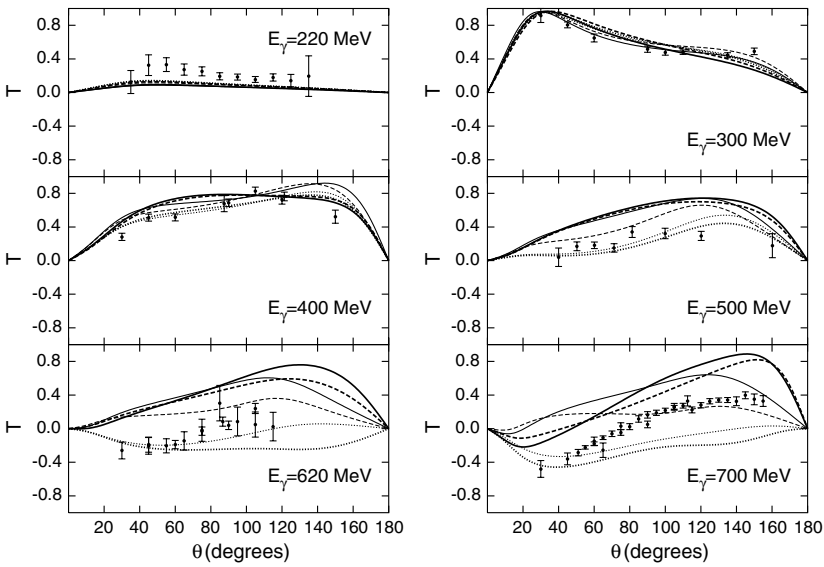

Fig. 23. Polarized target asymmetry of the $\gamma p \to \pi^+ n$ reaction. Experimental data are within the range $E_\gamma \pm 4$ MeV. Same conventions as in Fig. 10.

Quantitatively, the model provides satisfactory results nearly in the whole energy range and in almost every observable. Even in the cases where good quantitative result is not achieved, at least the qualitative behavior of data is well reproduced (i.e., Figs. 21 and 23).

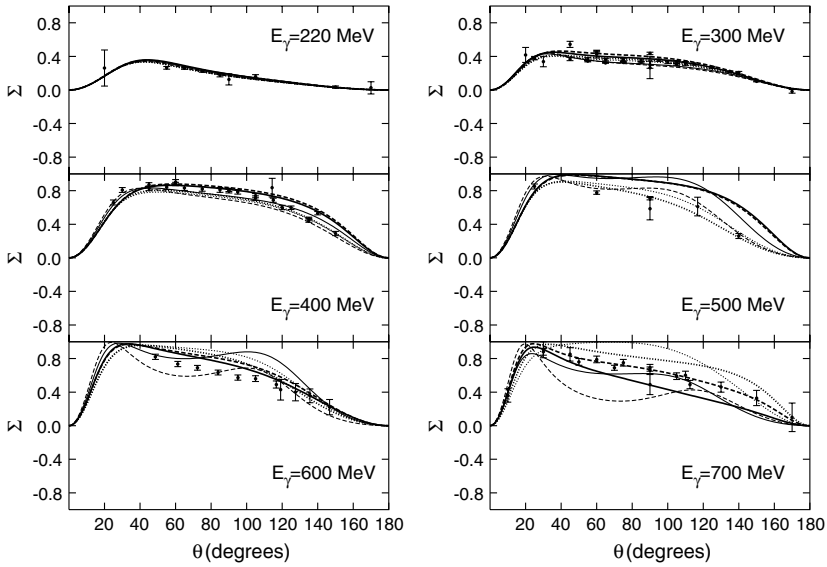

Fig. 24. Photon beam asymmetry of the $\gamma p \to \pi^+ n$ reaction. Experimental data are within the range $E_\gamma \pm 4$ MeV. Same conventions as in Fig. 10.

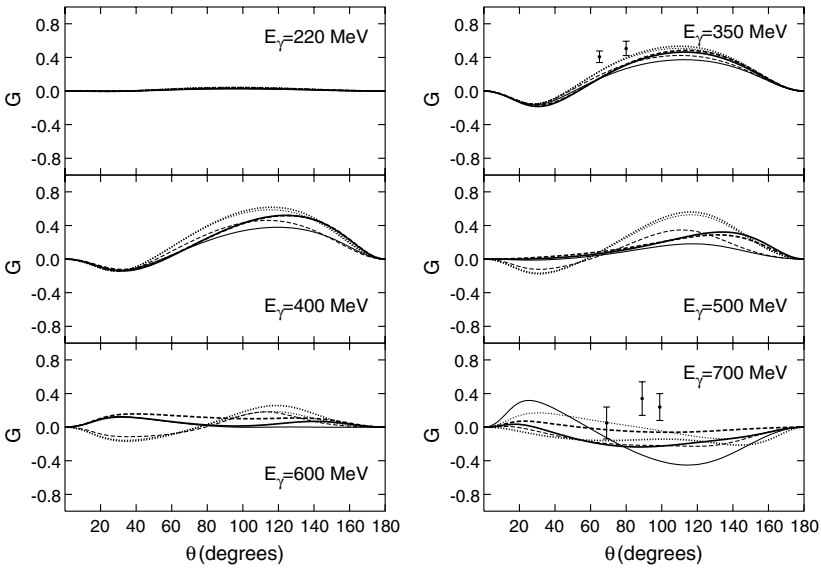

Fig. 25. G asymmetry of the $\gamma p \to \pi^+ n$ reaction. Experimental data are within the range $E_\gamma \pm 3$ MeV. Same conventions as in Fig. 10.

4.5. Cross-sections

Finally, in Fig. 33 we present results for the total cross-sections compared to available experimental data. The two upper figures show the total cross-section for charged pion channels and the two lower are for neutral pion photoproduction.

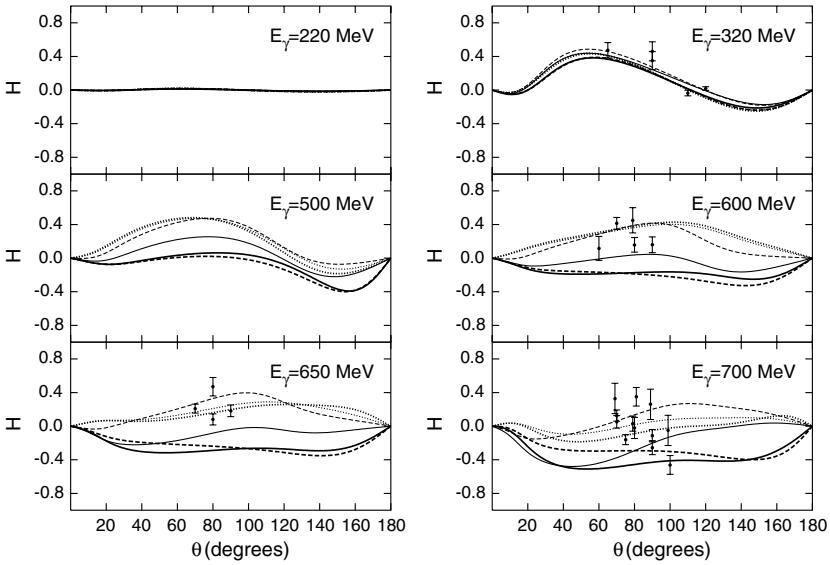

Fig. 26. H asymmetry of the $\gamma p \to \pi^+ n$ reaction. Experimental data are within the range $E_\gamma \pm 3$ MeV. Same conventions as in Fig. 10.

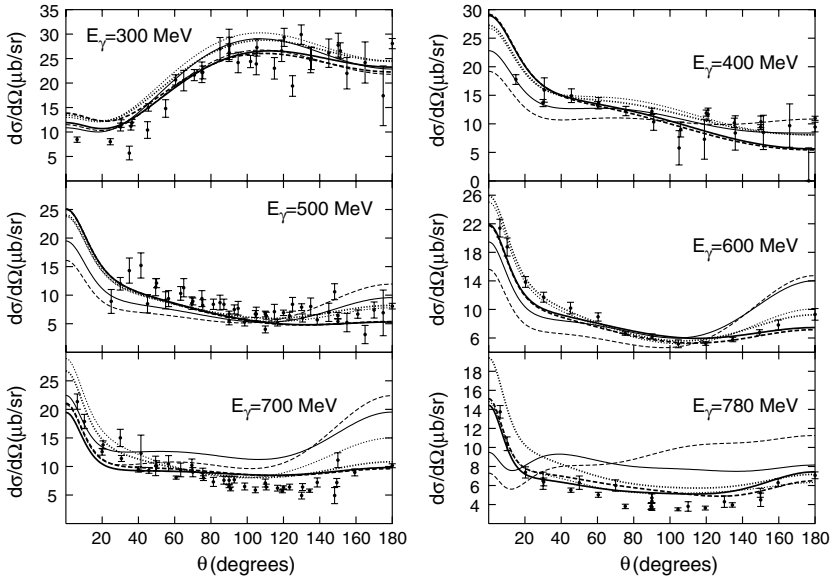

Fig. 27. Differential cross-section of the $\gamma p \to \pi^- p$ reaction. Experimental data are within the range $E_\gamma \pm 4$ MeV. Same conventions as in Fig. 8.

It is interesting to notice how some of the observed effects in the multipoles show up in the cross-sections. For example, sets #1, #4, and #5 overestimate the first resonance region due to the overestimation of $M_{1+}^{3/2}$ peak. On the other hand, set #4 presents a cusp

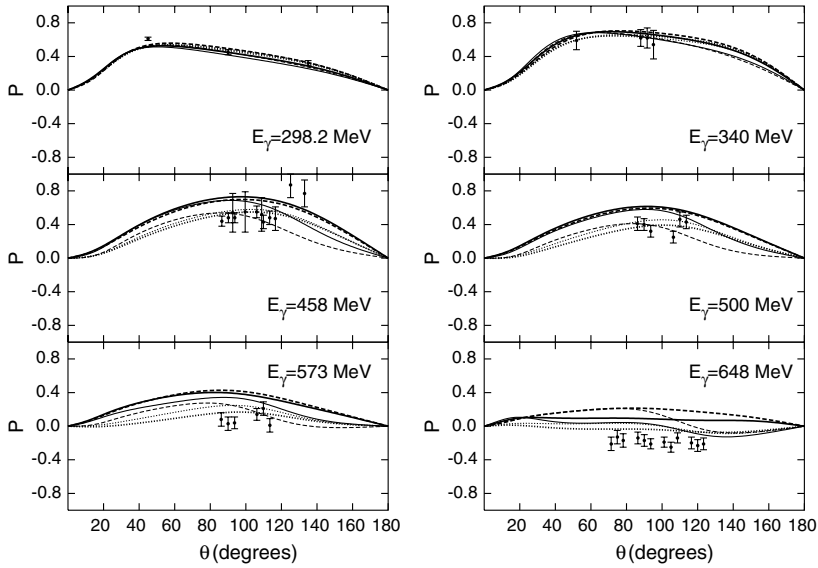

Fig. 28. Recoil nucleon polarization of the $\gamma p \to \pi^- p$ reaction. Experimental data are within the range $E_\gamma \pm 1$ MeV. Same conventions as in Fig. 10.

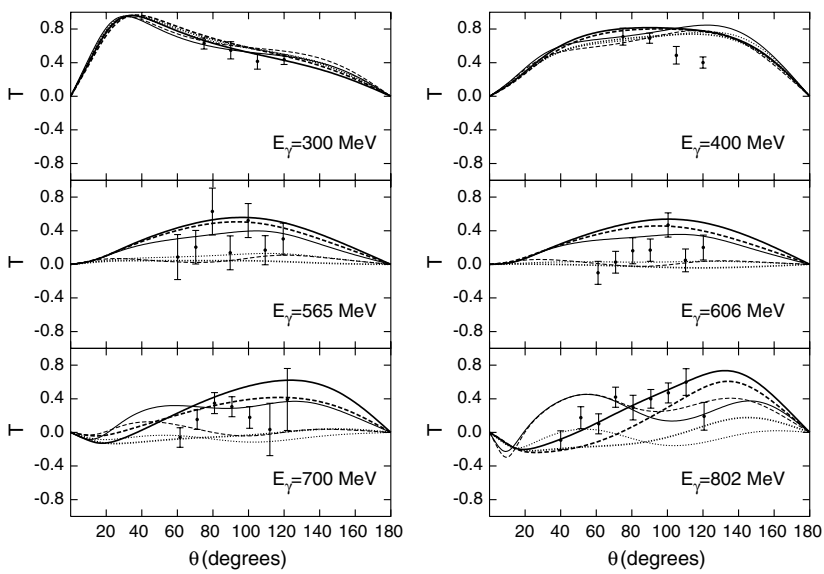

Fig. 29. Polarized target asymmetry of the $\gamma p \to \pi^- p$ reaction. Experimental data are within the range $E_\gamma \pm 5$ MeV. Same conventions as in Fig. 10.

peak in multipole $\mathrm{Im}\, E^{\mathrm{p}}_{0+}$, that also shows up in the cross-section, specially so in the $\pi^+ n$ channel. The high-energy behavior is well regularized. Nevertheless, it has to be considered that we do not take into account resonances D_{15} and F_{15} which may change the shape of the cross-section in the second resonance region.

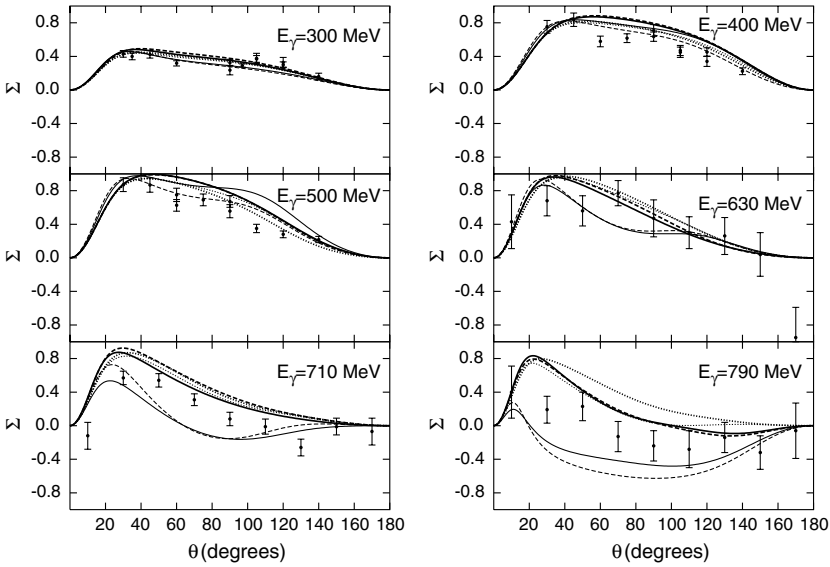

Fig. 30. Photon beam asymmetry of the $\gamma p \to \pi^- p$ reaction. Experimental data are within the range $E_\gamma \pm 1$ MeV. Same conventions as in Fig. 10.

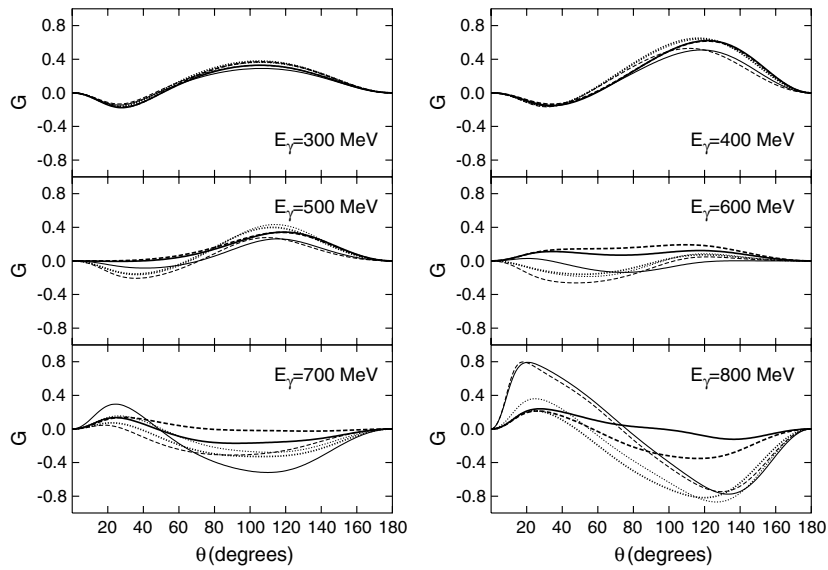

Fig. 31. G asymmetry of the $\gamma p \to \pi^- p$ reaction. Same conventions as in Fig. 10.

The low-energy behavior of the charged processes is quite well reproduced by all the sets of parameters. Actually, curves obtained with coupling constants from sets #1 and #2 agree quite well with data in almost the whole energy range. Other sets do not provide good results: sets #5 and #6 overestimate greatly the second resonance region for $\pi^- p$

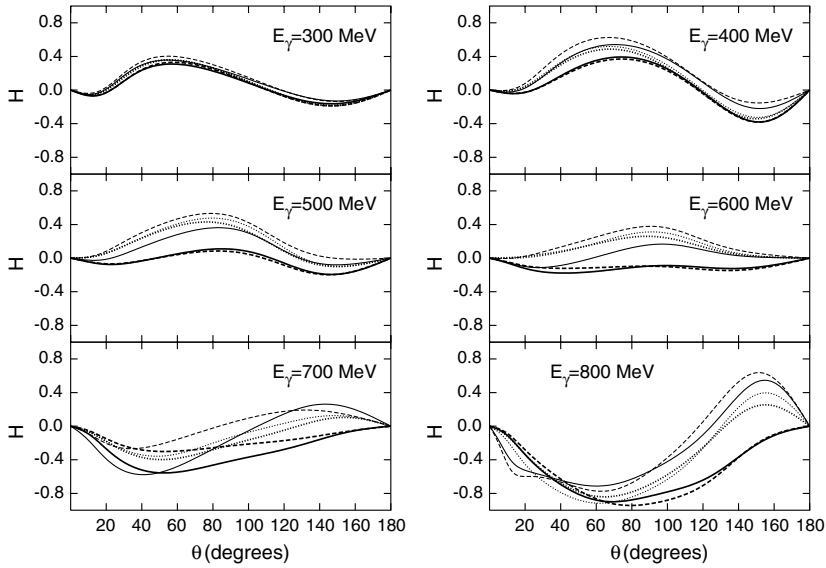

Fig. 32. H asymmetry of the $\gamma p \to \pi^- p$ reaction. Same conventions as in Fig. 10.

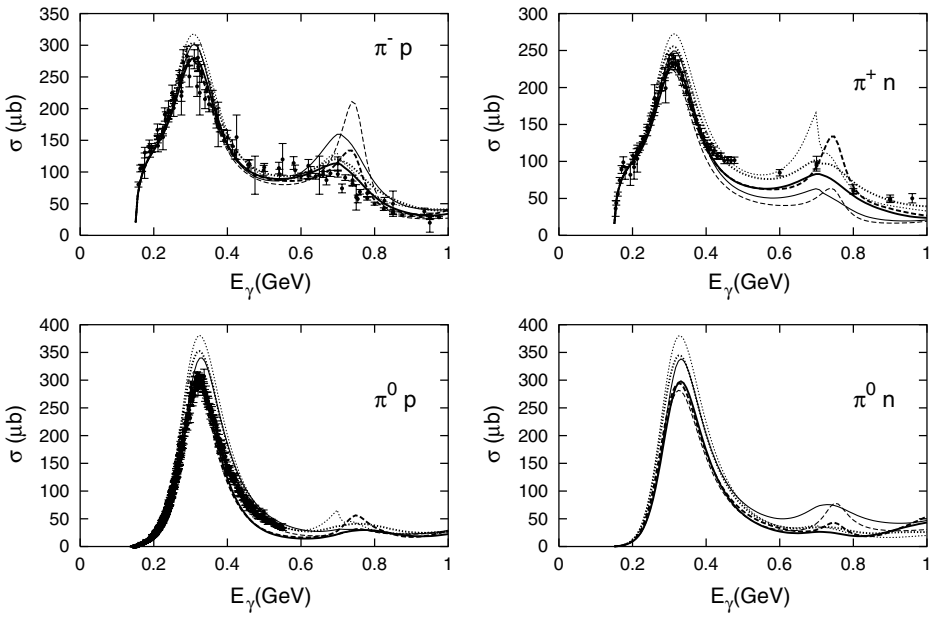

Fig. 33. Total cross-section as a function of photon energy in laboratory frame. Same curve conventions as in Fig. 8.

channel, and set #4 does the same in $\pi^+ n$ channel. Overestimation of the second resonance region by set #3 is due to the overestimation of multipoles related to resonance $N(1520)$.

Concerning the $\gamma n \to \pi^0 n$ channel we found several differences among sets either in the region of the first or in the region of the second resonance. As no data are available for $\pi^0 n$

total cross-sections, we rely on results on differential cross-section to infere that: up to 400 MeV, sets #2 and #3 may provide a good estimation of the total cross-section; and that beyond that energy, there may be probably an underestimation of the total cross-section.

In summary, we conclude that set #2 is the most reliable one because it provides the best results when all data are considered globally. We weigh that this is so, regardless of the fact that other sets may provide better fits to individual cases. For instance, set #6 provides the best fit to $\pi^0 p$ total cross-section and set #1 is very good for charged pion channels. As a matter of fact, set #2 has the lowest χ^2 for the electromagnetic multipoles. With this set the only deviations from experimental data in the total cross-section are the slight underestimation of $\pi^+ n$ and $\pi^0 p$ processes beyond 400 MeV.

5. Summary and final remarks

We have elaborated on a pion photoproduction model which is based on an Effective Lagrangian Approach (ELA) and is guided by Weinberg's theorem, fulfilling chiral symmetry, gauge invariance, and crossing symmetry. We have included Born terms, ρ and ω mesons exchange, and seven nucleon resonances: $\Delta(1232)$, $N(1440)$, $N(1520)$, $N(1535)$, $\Delta(1620)$, $N(1650)$, and $\Delta(1700)$. Under these premises, the model is independent of the underlying subnuclear physics (quarks, gluons), which is embedded in the parameters of the model, such as coupling constants, masses, and widths.

With respect to former models along similar lines, this is the first one that covers all the well-established spin-1/2 and spin-3/2 resonances up to 1.7 GeV and, at the same time, fulfills gauge invariance as well as chiral and crossing symmetries. Crossing symmetry could not be achieved in previous models such as the one of [12] due, among other things, to pathologies of former spin-3/2 Lagrangians. This problem is fixed in the present work by:

(a) the use of a spin-3/2 Lagrangian due to Pascalutsa that contains no spurious spin-1/2 components in the direct channel,
(b) the use of consistent, energy-dependent, strong couplings and widths, as well as form factors.

One of the goals of this paper is to establish a reliable set of parameters for the model. In addition to the cutoff Λ—which is related to short-distance effects and can be considered as the only free parameter of the model—we adjust electromagnetic coupling constants of the nucleon resonances within the usually accepted ranges. The determination of the parameters has been performed by fit to the experimental $\gamma p \to \pi^0 p$ multipoles, through a minimization procedure. In the minimization we have considered three different sets of masses and widths:

(a) Masses and widths taken from PDG with electromagnetic coupling constants within the PDG error bars.
(b) Masses and widths taken from the multichannel analysis of Vrana et al. [60] with electromagnetic coupling constants considered as free parameters.
(c) Masses and widths obtained by means of a speed plot calculation with the electromagnetic coupling constants considered as free parameters.

On the other hand, we have considered final state interactions (FSI) phenomenologically by adding an extra phase to the $\gamma p \to \pi^0 p$ multipoles, in order to match the current energy-dependent solution of SAID phases [4]. In all, we have derived six sets of parameters, one with and one without FSI for each of the abovementioned sets of masses and widths:

(a) Sets #1 and #4.
(b) Sets #2 and #5.
(c) Sets #3 and #6.

Electromagnetic multipoles for $\gamma p \to \pi^0 p$ are globally well reproduced by sets #1, #2, and #3 that include FSI. The fits without FSI (#4, #5, and #6) are also good in the low-energy regime. Other experimental observables are surveyed such as differential cross-section, asymmetries, and total cross-sections. At threshold we find good agreement with experimental data. In our model almost all the contribution at threshold comes from Born terms at variance with results in [12].

For charged pion production, where we have no adjustable parameters, the agreement is remarkably good for almost all the observables. We note that FSI phases obtained for the $\gamma p \to \pi^0 p$ process are not applicable to charged pion production. Thus, no FSI phases have been included in these charged pion photoproduction calculations. The fact that we get good agreement with data indicates that FSI are small in $\gamma p \to \pi^+ n$ and $\gamma n \to \pi^- p$.

Although all the parameter sets are reasonable, we favor set #2 because of its lowest χ^2 to the multipole data and its better agreement with the total cross-sections for all processes. Set #3, which also has a low χ^2, is very similar to set #2 and also yields similar helicity amplitudes for all the resonances except for $\Delta(1700)$. This resonance is poorly known and more precise information would be necessary. A better experimental knowledge of multipole $M_{2-}^{3/2}$ would improve the determination of the properties of $\Delta(1700)$ resonance. Similarly, better knowledge of the M_{1-}^{p} multipole would help to establish more reliably properties of $N(1440)$.

For the future, it would be interesting to analyze contributions from spin-5/2 nucleon resonances. Although they are not essential to the multipoles considered here, they may contribute to the background and their effect can be sizeable in the second resonance region of the total cross-section and asymmetries. The incorporation of the spin-5/2 resonances will require to take into account higher-order multipoles in the analysis. The inclusion of other resonances not considered here (three stars in PDG and *missing* resonances) could also improve the fits in some energy regions, but it is difficult to perform a reliable determination of the parameters without the aid of other physical processes where their contribution would be more sizeable.

The results obtained here are encouraging and stimulate the application of this model to other processes such as pion electroproduction, two pion production in nucleons and nuclei, as well as electro- and photoproduction of other mesons.

Acknowledgments

One of us (C.F.-R.) thanks Professor H. Garcilazo and Professor R.A. Arndt for useful comments, and Dr. V. Pascalutsa and Professor W. Weise for useful discussions. C.F.-R. work is being developed under Spanish Government Grant UAC2002-0009. This work has been supported in part under contracts of Ministerio de Educación y Ciencia (Spain) BFM2002-03562 and BFM2003-04147-C02-01.

Appendix A. Invariant amplitudes

In this appendix, we show all the invariant amplitudes needed for the calculations in the isospin decomposition and the notation for kinematics of Section 2. We name v to the four momentum of the exchanged particle in each diagram.

A.1. Born amplitudes

- s-channel (diagram A in Fig. 1)

$$A_s^0 = -\frac{ef_{\pi N}}{2m_\pi}\bar{u}(p')\not{k}\gamma_5\frac{\not{p}+M}{s-M^2}\left[\not{A}F_1^{\mathrm{S}} - \frac{F_2^{\mathrm{S}}}{2M}A^\alpha\gamma_{\alpha\beta}q^\beta\right]u(p), \tag{A.1}$$

$$A_s^- = A_s^+ = A_s^0\left(F_1^{\mathrm{S}} \to F_1^{\mathrm{V}}, F_2^{\mathrm{S}} \to F_2^{\mathrm{V}}\right). \tag{A.2}$$

- u-channel (diagram B in Fig. 1)

$$A_u^0 = -\frac{ef_{\pi N}}{2m_\pi}\bar{u}(p')\left[\not{A}F_1^{\mathrm{S}} - \frac{F_2^{\mathrm{S}}}{2M}A^\alpha\gamma_{\alpha\beta}q^\beta\right]\frac{\not{p}+M}{u-M^2}\not{k}\gamma_5 u(p), \tag{A.3}$$

$$A_u^+ = -A_u^- = A_u^0\left(F_1^{\mathrm{S}} \to F_1^{\mathrm{V}}, F_2^{\mathrm{S}} \to F_2^{\mathrm{V}}\right). \tag{A.4}$$

- t-channel (diagram C in Fig. 1)

$$A_t^- = -eF_1^{\mathrm{V}}\frac{f_{\pi N}}{m_\pi}\bar{u}(p')\frac{A\cdot(v+k)}{t-m_\pi^2}\not{p}\gamma_5 u(p). \tag{A.5}$$

- Kroll–Rudermann (contact) term (diagram D in Fig. 1)

$$A_{KR}^- = eF_1^{\mathrm{V}}\frac{f_{\pi N}}{m_\pi}\bar{u}(p')\not{A}\gamma_5 u(p). \tag{A.6}$$

A.2. Vector meson amplitudes

- ρ meson (diagram F in Fig. 2)

$$A_\rho^0 = -\mathrm{i}e\frac{G_{\rho\pi\gamma}F_{\rho NN}}{m_\pi}\bar{u}(p')\frac{\epsilon_{\sigma\lambda\nu\mu}q^\sigma k^\nu A^\lambda g^{\alpha\mu}}{t-m_\rho^2}\left[\gamma_\alpha + \frac{K_\rho}{2M}\gamma_{\alpha\beta}v^\beta\right]u(p). \tag{A.7}$$

- ω meson (diagram F in Fig. 2)

$$A_\omega^+ = -\mathrm{i}e\frac{G_{\omega\pi\gamma}F_{\omega NN}}{m_\pi}\bar{u}(p')\frac{\epsilon_{\sigma\lambda\nu\mu}q^\sigma k^\nu A^\lambda g^{\alpha\mu}}{t-m_\omega^2}\left[\gamma_\alpha + \frac{K_\omega}{2M}\gamma_{\alpha\beta}v^\beta\right]u(p). \tag{A.8}$$

A.3. S_{11} resonance amplitudes

- s-channel

$$A_{s,\mathrm{S}_{11}}^0 = \frac{eg_{\mathrm{S}}h}{2Mf_\pi}\bar{u}(p')\not{k}G(v)A^\mu\gamma_{\mu\nu}q^\nu\gamma_5 u(p), \tag{A.9}$$

$$A^{+}_{s,\mathrm{S}_{11}} = A^{-}_{s,\mathrm{S}_{11}} = A^{0}_{s,\mathrm{S}_{11}}(g_{\mathrm{S}} \to g_{\mathrm{V}}). \tag{A.10}$$

- u-channel

$$A^{0}_{u,\mathrm{S}_{11}} = -\frac{eg_{\mathrm{S}}h}{2Mf_{\pi}}\bar{u}(p')A^{\mu}\gamma_{\mu\nu}q^{\nu}\gamma_5 G(v)\not{k}u(p), \tag{A.11}$$

$$A^{+}_{u,\mathrm{S}_{11}} = -A^{-}_{u,\mathrm{S}_{11}} = A^{0}_{u,\mathrm{S}_{11}}(g_{\mathrm{S}} \to g_{\mathrm{V}}). \tag{A.12}$$

A.4. S_{31} resonance amplitudes

- s-channel

$$A^{+}_{s,\mathrm{S}_{31}} = -2A^{-}_{s,\mathrm{S}_{31}} = \frac{2}{3}\frac{egh}{Mf_{\pi}}\bar{u}(p')\not{k}G(v)A^{\mu}\gamma_{\mu\nu}q^{\nu}\gamma_5 u(p), \tag{A.13}$$

- u-channel

$$A^{+}_{u,\mathrm{S}_{31}} = 2A^{-}_{u,\mathrm{S}_{31}} = -\frac{2}{3}\frac{egh}{Mf_{\pi}}\bar{u}(p')A^{\mu}\gamma_{\mu\nu}q^{\nu}\gamma_5 G(v)\not{k}u(p). \tag{A.14}$$

A.5. P_{11} resonance amplitudes

- s-channel

$$A^{0}_{s,\mathrm{P}_{11}} = \frac{eg_{\mathrm{S}}h}{2Mf_{\pi}}\bar{u}(p')\not{k}\gamma_5 G(v)A^{\mu}\gamma_{\mu\nu}q^{\nu}u(p), \tag{A.15}$$

$$A^{+}_{s,\mathrm{P}_{11}} = A^{-}_{s,\mathrm{P}_{11}} = A^{0}_{s,\mathrm{P}_{11}}(g_{\mathrm{S}} \to g_{\mathrm{V}}). \tag{A.16}$$

- u-channel

$$A^{0}_{u,\mathrm{P}_{11}} = \frac{eg_{\mathrm{S}}h}{2Mf_{\pi}}\bar{u}(p')A^{\mu}\gamma_{\mu\nu}q^{\nu}G(v)\not{k}\gamma_5 u(p), \tag{A.17}$$

$$A^{+}_{u,\mathrm{P}_{11}} = -A^{-}_{u,\mathrm{P}_{11}} = A^{0}_{u,\mathrm{P}_{11}}(g_{\mathrm{S}} \to g_{\mathrm{V}}). \tag{A.18}$$

A.6. P_{33} resonance amplitudes

- s-channel

$$\begin{aligned} A^{+}_{s,\mathrm{P}_{33}} = -2A^{-}_{s,\mathrm{P}_{33}} &= \frac{-\mathrm{i}he}{f_{\pi}M^{*}M(M^{*}+M)}\bar{u}(p')\epsilon_{\mu\nu\lambda\beta}v^{\mu}k^{\lambda}\gamma^{\beta}\gamma^{5}G^{\nu\alpha}(v) \\ &\quad \times \left[\mathrm{i}g_1\epsilon_{\omega\alpha\rho\phi}v^{\omega}q^{\rho}A^{\phi} + g_2\gamma^5(v\cdot qA_{\alpha} - v\cdot Aq_{\alpha})\right]u(p). \end{aligned} \tag{A.19}$$

- u-channel

$$A^{+}_{u,\mathrm{P}_{33}} = 2A^{-}_{u,\mathrm{P}_{33}} = \frac{\mathrm{i}he}{f_\pi M^* M(M^*+M)}\bar{u}(p')$$
$$\times\left[\mathrm{i}g_1\epsilon_{\mu\nu\alpha\beta}v^\mu q^\alpha A^\beta + g_2\gamma^5(v\cdot qA_\nu - v\cdot Aq_\nu)\right]G^{\nu\phi}(v)\epsilon_{\omega\phi\lambda\rho}v^\omega k^\lambda\gamma^\rho\gamma^5 u(p). \quad \text{(A.20)}$$

A.7. D_{33} resonance amplitudes

- s-channel

$$A^{+}_{s,\mathrm{D}_{33}} = -2A^{-}_{s,\mathrm{D}_{33}} = \frac{\mathrm{i}he}{f_\pi MM^*(M+M^*)}\bar{u}(p')\epsilon_{\mu\nu\lambda\beta}v^\mu k^\lambda\gamma^\beta G^{\lambda\alpha}(v)$$
$$\times\left[\mathrm{i}g_1\epsilon_{\omega\alpha\rho\phi}v^\omega q^\rho A^\phi\gamma^5 + g_2(v\cdot qA_\alpha - v\cdot Aq_\alpha)\right]u(p). \quad \text{(A.21)}$$

- u-channel

$$A^{+}_{u,\mathrm{D}_{33}} = 2A^{-}_{u,\mathrm{D}_{33}} = \frac{\mathrm{i}eh}{f_\pi MM^*(M+M^*)}\bar{u}(p')$$
$$\times\left[\mathrm{i}g_1\epsilon_{\mu\nu\alpha\beta}q^\alpha v^\mu A^\beta\gamma^5 + g_2(v\cdot qA_\nu - v\cdot Aq_\nu)\right]G^{\nu\lambda}(v)\epsilon_{\omega\lambda\rho\phi}v^\omega k^\rho\gamma^\phi u(p). \quad \text{(A.22)}$$

A.8. D_{13} resonance amplitudes

- s-channel

$$A^{0}_{s,\mathrm{D}_{13}} = \frac{3\mathrm{i}he}{4f_\pi MM^*(M+M^*)}\bar{u}(p')\epsilon_{\mu\nu\lambda\beta}v^\mu k^\lambda\gamma^\beta G^{\lambda\alpha}(v)$$
$$\times\left[\mathrm{i}g^{\mathrm{S}}_1\epsilon_{\omega\alpha\rho\phi}v^\omega q^\rho A^\phi\gamma^5 + g^{\mathrm{S}}_2(v\cdot qA_\alpha - v\cdot Aq_\alpha)\right]u(p), \quad \text{(A.23)}$$
$$A^{+}_{s,\mathrm{D}_{13}} = A^{-}_{s,\mathrm{D}_{13}} = A^{0}_{s,\mathrm{D}_{13}}\left(g^{\mathrm{S}}_{1,2}\to g^{\mathrm{V}}_{1,2}\right). \quad \text{(A.24)}$$

- u-channel

$$A^{0}_{u,\mathrm{D}_{13}} = \frac{3\mathrm{i}eh}{4f_\pi MM^*(M+M^*)}\bar{u}(p')$$
$$\times\left[\mathrm{i}g^{\mathrm{S}}_1\epsilon_{\mu\nu\alpha\beta}q^\alpha v^\mu A^\beta\gamma^5 + g^{\mathrm{S}}_2(v\cdot qA_\nu - v\cdot Aq_\nu)\right]G^{\nu\lambda}(v)\epsilon_{\omega\lambda\rho\phi}v^\omega k^\rho\gamma^\phi u(p), \quad \text{(A.25)}$$
$$A^{+}_{u,\mathrm{D}_{13}} = -A^{-}_{u,\mathrm{D}_{13}} = A^{0}_{u,\mathrm{D}_{13}}\left(g^{\mathrm{S}}_{1,2}\to g^{\mathrm{V}}_{1,2}\right). \quad \text{(A.26)}$$

Appendix B. Decay widths

The coupling constants at the strong vertices are related to the decay widths of the resonances. Given the following kinematical definitions

$$k^* = \frac{1}{2M^*}\left[(M^{*2}-M^2-m_\pi^2)^2 - 4m_\pi^2M^2\right]^{\frac{1}{2}}, \quad \text{(B.1)}$$
$$E_\pi = \sqrt{k^{*2}+m_\pi^2}, \quad \text{(B.2)}$$
$$E_N = \sqrt{k^{*2}+M^2}, \quad \text{(B.3)}$$

the decay widths related to the resonance Lagrangians of Section 3 are

$$\Gamma_\pi^{S_{11}} = 3\frac{k^* h^2}{2\pi M^* f_\pi^2}\frac{\left[E_\pi(E_N+M)+k^{*2}\right]^2}{2(E_N+M)}, \tag{B.4}$$

$$\Gamma_\pi^{S_{31}} = \frac{k^* h^2}{2\pi M^* f_\pi^2}\frac{\left[E_\pi(E_N+M)+k^{*2}\right]^2}{2(E_N+M)}, \tag{B.5}$$

$$\Gamma_\pi^{P_{11}} = 3\frac{k^{*3} h^2}{2\pi M^* f_\pi^2}\frac{(E_N+M+E_\pi)^2}{2(E_N+M)}, \tag{B.6}$$

$$\Gamma_\pi^{P_{33}} = \frac{h^2}{3\pi f_\pi^2}\frac{k^{*3}}{M^*}(E_N+M), \tag{B.7}$$

$$\Gamma_\pi^{D_{33}} = \frac{h^2}{3\pi f_\pi^2}\frac{k^{*5}}{M^*}\frac{1}{E_N+M}, \tag{B.8}$$

$$\Gamma_\pi^{D_{13}} = \frac{h^2}{\pi f_\pi^2}\frac{k^{*5}}{M^*}\frac{1}{E_N+M}. \tag{B.9}$$

Appendix C. Electromagnetic multipoles

The starting point for multipole analysis is to define the helicity spinors in the c.m. reference system for incoming,

$$u(p)^{\lambda=\frac{1}{2}} = \sqrt{\rho}\begin{bmatrix}0\\1\\0\\\zeta\end{bmatrix}, \qquad u(p)^{\lambda=-\frac{1}{2}} = \sqrt{\rho}\begin{bmatrix}1\\0\\-\zeta\\0\end{bmatrix}; \tag{C.1}$$

and outgoing nucleons,

$$\bar{u}(p')^{\lambda=\frac{1}{2}} = \sqrt{\rho'}\left[-\sin\frac{\theta}{2}, \cos\frac{\theta}{2}, \zeta'\sin\frac{\theta}{2}, -\zeta'\cos\frac{\theta}{2}\right], \tag{C.2}$$

$$\bar{u}(p')^{\lambda=-\frac{1}{2}} = \sqrt{\rho'}\left[\cos\frac{\theta}{2}, \sin\frac{\theta}{2}, \zeta'\cos\frac{\theta}{2}, \zeta'\sin\frac{\theta}{2}\right]; \tag{C.3}$$

where $\rho = E^* + M$, $\rho' = E'^* + M$, $\zeta = \frac{q^*}{\rho}$, and $\zeta' = \frac{k^*}{\rho'}$.

All formulae in this and forthcoming appendices are in c.m. reference system and with this spinors definition.

To build up the multipoles it is convenient to change the isospin basis from (A^0, A^+, A^-) to $(A^{3/2}, {}_pA^{1/2}, {}_nA^{1/2})$. Both bases are related by means of

$$A^{3/2} = A^+ - A^-, \tag{C.4}$$

$${}_pA^{1/2} = \tfrac{1}{3}A^+ + \tfrac{2}{3}A^- + A^0, \tag{C.5}$$

$${}_nA^{1/2} = -\tfrac{1}{3}A^+ - \tfrac{2}{3}A^- + A^0. \tag{C.6}$$

Defining $\lambda = \lambda_\gamma - \lambda_1$, initial helicity state along the photon, and $\mu = -\lambda_2$, final helicity state along the pion, the spin and isospin projection of amplitudes can be written as

$$H^{I,j}_{\lambda\mu}(W) = \frac{1}{8W\pi}\int_{-1}^{1} d(\cos\theta) d^{j}_{\lambda\mu}(\theta) A^{I}_{\lambda\mu}(\theta, W), \tag{C.7}$$

where $W = \sqrt{s^*}$, j is the spin of the resonance, and $d^{j}_{\lambda\mu}(\theta)$ are Wigner d-functions with the conventions of [30]. The lowest-order multipole amplitudes are [2,8,71]:

$$E^{I}_{0+} = \frac{\sqrt{2}}{4}\left[H^{I,1/2}_{1/2,1/2} + H^{I,1/2}_{1/2,-1/2}\right], \tag{C.8}$$

$$M^{I}_{1-} = -\frac{\sqrt{2}}{4}\left[H^{I,1/2}_{1/2,1/2} - H^{I,1/2}_{1/2,-1/2}\right], \tag{C.9}$$

$$E^{I}_{1+} = \frac{\sqrt{2}}{8}\left[\left(H^{I,3/2}_{1/2,1/2} + H^{I,3/2}_{1/2,-1/2}\right) - \frac{1}{\sqrt{3}}\left(H^{I,3/2}_{3/2,1/2} + H^{I,3/2}_{3/2,-1/2}\right)\right], \tag{C.10}$$

$$M^{I}_{1+} = \frac{\sqrt{2}}{8}\left[\left(H^{I,3/2}_{1/2,1/2} + H^{I,3/2}_{1/2,-1/2}\right) + \sqrt{3}\left(H^{I,3/2}_{3/2,1/2} + H^{I,3/2}_{3/2,-1/2}\right)\right], \tag{C.11}$$

$$E^{I}_{2-} = \frac{\sqrt{2}}{8}\left[\left(H^{I,3/2}_{1/2,1/2} - H^{I,3/2}_{1/2,-1/2}\right) + \sqrt{3}\left(H^{I,3/2}_{3/2,1/2} - H^{I,3/2}_{3/2,-1/2}\right)\right], \tag{C.12}$$

$$M^{I}_{2-} = -\frac{\sqrt{2}}{8}\left[\left(H^{I,3/2}_{1/2,1/2} - H^{I,3/2}_{1/2,-1/2}\right) - \frac{1}{\sqrt{3}}\left(H^{I,3/2}_{3/2,1/2} - H^{I,3/2}_{3/2,-1/2}\right)\right]. \tag{C.13}$$

Appendix D. Experimental helicity amplitudes

In this appendix we present the connection between our amplitudes and the helicity amplitudes of the resonances as they are found in [30] to relate the coupling constants to the usual partial wave analyses. To perform this connection the isospin decomposition $(A^{\Delta}, A^{p}, A^{n})$ is needed instead of the one in Section 2. Both are related in the following way

$$A^{\Delta} = \sqrt{\frac{2}{3}}(A^{+} - A^{-}), \tag{D.1}$$

$$A^{\mathrm{p}} = -\frac{1}{\sqrt{3}}(A^{+} + 2A^{-} + 3A^{0}), \tag{D.2}$$

$$A^{\mathrm{n}} = \frac{1}{\sqrt{3}}(A^{+} + 2A^{-} - 3A^{0}). \tag{D.3}$$

And the helicity amplitudes are given by [12,72]

$$A^{I}_{\lambda} d^{j}_{\lambda\mu}(\theta) = \frac{\mathrm{i}}{8\pi(2j+1)}\sqrt{(2j+1)\frac{2\pi}{s^*}\frac{k^*}{q^*}\frac{M^*}{M}\frac{\Gamma^2}{\Gamma_\pi}} A^{I}_{\lambda_1\lambda_2\lambda_\gamma}, \tag{D.4}$$

where λ, μ, j, and $d^{j}_{\lambda\mu}(\theta)$ have the same meaning as in Appendix C; Γ is the total decay width and Γ_π the pion–nucleon decay width of the resonance as defined in Appendix B. k^* and q^* are the pion and the photon momenta in the c.m. system. We define the kinematical coefficients

$$q^* = \frac{M^{*2} - M^2}{2M^*}, \tag{D.5}$$

$$\xi = \frac{q^*}{\sqrt{q^{*2} + M^2} + M}, \tag{D.6}$$

$$T = \frac{1}{4}\frac{M^*}{M(M+M^*)}\frac{q^*}{\sqrt{M\xi}}, \tag{D.7}$$

to obtain finally the following results:

- Resonance S_{11}

$$A^{p,n}_{1/2}(S_{11}) = \frac{1}{\sqrt{2}}\frac{eg^{p,n}}{M}\sqrt{\frac{\xi}{M}}(M+M^*). \tag{D.8}$$

- Resonance S_{31}

$$A^{\Delta}_{1/2}(S_{31}) = -\frac{1}{\sqrt{3}}\frac{eg}{M}\sqrt{\frac{\xi}{M}}(M+M^*). \tag{D.9}$$

- Resonance P_{11}

$$A^{p,n}_{1/2}(P_{11}) = -\frac{1}{\sqrt{2}}\frac{eg^{p,n}}{M}\sqrt{\frac{\xi}{M}}(M+M^*). \tag{D.10}$$

- Resonance P_{33}

$$A^{\Delta}_{1/2}(P_{33}) = -eT\sqrt{\frac{1}{2}}[g_1 - \xi g_2], \tag{D.11}$$

$$A^{\Delta}_{3/2}(P_{33}) = -eT\sqrt{\frac{3}{2}}[g_1 + \xi g_2]. \tag{D.12}$$

- Resonance D_{33}

$$A^{\Delta}_{1/2}(D_{33}) = eT\frac{\sqrt{2}}{2}[g_2 - \xi g_1], \tag{D.13}$$

$$A^{\Delta}_{3/2}(D_{33}) = eT\sqrt{\frac{3}{2}}[g_2 + \xi g_1]. \tag{D.14}$$

- Resonance D_{13}

$$A^{p,n}_{1/2}(D_{13}) = -eT\frac{3}{2\sqrt{3}}[g^{p,n}_2 - \xi g^{p,n}_1], \tag{D.15}$$

$$A^{p,n}_{3/2}(D_{13}) = -eT\frac{3}{2}[g^{p,n}_2 + \xi g^{p,n}_1]. \tag{D.16}$$

References

[1] B. Krusche, S. Schadmand, Prog. Part. Nucl. Phys. 51 (2003) 399–485.
[2] R.A. Arndt, R.L. Workman, Z. Li, L.D. Roper, Phys. Rev. C 42 (1990) 1853–1863.

[3] R.A. Arndt, I.I. Strakovsky, R.L. Workman, Phys. Rev. C 53 (1996) 430–440;
R.A. Arndt, W.J. Briscoe, I.I. Strakovsky, R.L. Workman, Phys. Rev. C 66 (2002) 055213.
[4] R.A. Arndt, W.J. Briscoe, R.L. Workman, I.I. Strakovsky, SAID database. <http://gwdac.phys.gwu.edu/>.
[5] A. Shafi et al., Phys. Rev. C 70 (2004) 035204.
[6] G. Blanpied et al., Phys. Rev. C 64 (2001) 025203.
[7] C. Molinari et al., Phys. Lett. B 371 (1996) 181–185;
J. Peise et al., Phys. Lett. B 384 (1996) 37–42;
R. Beck et al., Phys. Rev. Lett. 78 (1997) 606–609;
F. Wissmann et al., Nucl. Phys. A 660 (1999) 232–245;
B. Krusche et al., Eur. Phys. J. A 22 (2004) 277–291.
[8] R.L. Walker, Phys. Rev. 182 (1969) 1729–1748.
[9] D. Drechsel, O. Hanstein, S.S. Kamalov, L. Tiator, Nucl. Phys. A 645 (1999) 145–174, <http://www.kph.uni-mainz.de/MAID//>.
[10] M.G. Olsson, Nucl. Phys. B 78 (1974) 55–76;
M.G. Olsson, E.T. Osypowski, Phys. Rev. D 17 (1978) 174–184.
[11] R.M. Davidson, N.C. Mukhopadhyay, R.S. Wittman, Phys. Rev. D 43 (1991) 71–94.
[12] H. Garcilazo, E. Moya de Guerra, Nucl. Phys. A 562 (1993) 521–568.
[13] T. Feuster, U. Mosel, Nucl. Phys. A 612 (1997) 375–390.
[14] M. Vanderhaeghen, K. Heyde, J. Ryckebusch, M. Waroquier, Nucl. Phys. A 595 (1995) 219–258.
[15] O. Scholten, A.Yu. Korchin, V. Pascalutsa, D. Van Neck, Phys. Lett. B 384 (1996) 13–19.
[16] S. Nozawa, B. Blankleider, T.-S.H. Lee, Nucl. Phys. A 513 (1990) 459–510.
[17] T. Sato, T.-S.H. Lee, Phys. Rev. C 54 (1996) 2660–2684;
T. Sato, T.-S.H. Lee, Phys. Rev. C 63 (2001) 055201.
[18] M.G. Fuda, H. Alharbi, Phys. Rev. C 68 (2003) 064002.
[19] V. Pascalutsa, J.A. Tjon, Phys. Rev. C 70 (2004) 035209.
[20] I.G. Aznauryan, Phys. Rev. C 67 (2003) 015209.
[21] Z.-P. Li, H.-X. Ye, M.-H. Lu, Phys. Rev. C 56 (1997) 1099–1113;
Q. Zhao, J.S. Al-Khalili, Z.-P. Li, R.L. Workman, Phys. Rev. C 65 (2002) 065204.
[22] V. Bernard, N. Kaiser, U.-G. Meißner, Int. J. Mod. Phys. E 4 (1995) 193–344.
[23] V. Bernard, N. Kaiser, U.-G. Meißner, Nucl. Phys. B 383 (1992) 442–496.
[24] A.W. Thomas, W. Weise, The Structure of the Nucleon, Wiley-VCH, Berlin, 2001.
[25] H. Garcilazo, E. Moya de Guerra, Phys. Rev. C 49 (1994) R601–R604;
H. Garcilazo, E. Moya de Guerra, Phys. Rev. C 52 (1995) 49–60.
[26] S. Karataglidis, C. Benhold, Phys. Rev. Lett. 80 (1998) 1614–1617.
[27] J.A. Gómez Tejedor, E. Oset, Nucl. Phys. A 571 (1994) 667–693;
J.A. Gómez Tejedor, E. Oset, Nucl. Phys. A 600 (1996) 413–435.
[28] J. Dubach, J.H. Koch, T.W. Donnelly, Nucl. Phys. A 271 (1976) 279–316;
J.W. Van Orden, T.W. Donnelly, Ann. Phys. (N.Y.) 131 (1981) 451–493;
M.J. Dekker, P.J. Brussaard, J.A. Tjon, Phys. Rev. C 49 (1994) 2650–2670;
J.E. Amaro, M.B. Barbaro, J.A. Caballero, T.W. Donnelly, A. Molinari, Nucl. Phys. A 697 (2002) 388–428;
J.E. Amaro, M.B. Barbaro, J.A. Caballero, T.W. Donnelly, A. Molinari, Phys. Rep. 368 (2002) 317–407.
[29] V. Pascalutsa, Phys. Rev. D 58 (1998) 096002.
[30] S. Eidelman et al., Phys. Lett. B 592 (2004) 1–1109.
[31] F. Halzen, A.D. Martin, Quarks and Leptons: An Introductory Course in Modern Particle Physics, Wiley, New York, 1984.
[32] S. Weinberg, Physica A 96 (1979) 327–340.
[33] H. Leutwyler, Ann. Phys. (N.Y.) 235 (1994) 165–203.
[34] R.A. Arndt, Z. Li, L.D. Roper, Phys. Rev. Lett. 65 (1990) 157–158;
J.R. Bergervoet, P.C. van Campen, R.A.M. Klomp, J.-L. de Kok, T.A. Rijken, V.G.J. Stocks, J.J. de Swart, Phys. Rev. C 41 (1990) 1435–1452.
[35] R.D. Peccei, Phys. Rev. 176 (1968) 1812–1821;
R.D. Peccei, Phys. Rev. 181 (1969) 1902–1905.
[36] L.M. Nath, B. Etemadi, J.D. Kimel, Phys. Rev. D 3 (1971) 2153–2161.
[37] W. Greiner, Relativistic Quantum Mechanics—Wave Equations, Springer-Verlag, Berlin, 1997.
[38] M. Benmerrouche, R.M. Davidson, N.C. Mukhopadhyay, Phys. Rev. C 39 (1989) 2339–2348.
[39] V. Pascalutsa, Phys. Lett. B 503 (2001) 85–90.

[40] V. Pascalutsa, R. Timmermans, Phys. Rev. C 60 (1999) 042201.
[41] W. Rarita, J. Schwinger, Phys. Rev. 60 (1941) 61.
[42] T. Feuster, U. Mosel, Phys. Rev. C 58 (1998) 457–488.
[43] V. Pascalutsa, O. Scholten, Nucl. Phys. A 591 (1995) 658–674.
[44] K. Johnson, E.C.G. Sudarshan, Ann. Phys. (N.Y.) 13 (1961) 126–145.
[45] C.R. Hagen, Phys. Rev. D 4 (1971) 2204–2208;
L.P.S. Singh, Phys. Rev. D 7 (1973) 1256–1258.
[46] G. Velo, D. Zwanziger, Phys. Rev. 186 (1969) 1337–1341;
G. Velo, D. Zwanziger, Phys. Rev. 188 (1969) 2218–2222.
[47] C. Fronsdal, Phys. Rev. D 18 (1978) 3624–3629.
[48] J. Fang, C. Fronsdal, Phys. Rev. D 18 (1978) 3630–3633.
[49] T. Curtright, Phys. Lett. B 85 (1979) 219–224;
B. de Wit, D.Z. Freedman, Phys. Rev. D 21 (1980) 358–367.
[50] S. Weinberg, The Quantum Theory Of Fields, Vol. I: Foundations, Cambridge University Press, Cambridge, England, 1995.
[51] S. Weinberg, E. Witten, Phys. Lett. B 503 (1980) 59–62.
[52] H.F. Jones, M.D. Scadron, Ann. Phys. (N.Y.) 81 (1973) 1–14.
[53] F. Ernst, R. Sachs, K. Wali, Phys. Rev. 119 (1960) 1105–1114.
[54] V. Pascalutsa, D.R. Phillips, Phys. Rev. C 67 (2003) 055202.
[55] S. Kondratyuk, O. Scholten, Phys. Rev. C 64 (2001) 024005.
[56] S. Kondratyuk, O. Scholten, Phys. Rev. C 62 (2000) 025203.
[57] R.M. Davidson, R. Workman, Phys. Rev. C 63 (2001) 058201;
R.M. Davidson, R. Workman, Phys. Rev. C 63 (2001) 025210.
[58] P. Mergell, Ulf-G. Meißner, D. Drechsel, Nucl. Phys. A 596 (1996) 367–396.
[59] O. Gayou et al., Phys. Rev. Lett. 88 (2003) 092301;
W. Wu et al., Phys. Rev. C 67 (2003) 012201(R).
[60] T.P. Vrana, S.A. Dytman, T.-S.H. Lee, Phys. Rep. 328 (2000) 181–236.
[61] G. Höhler, Eur. Phys. J. C 3 (1998) 1–794, p. 624, and references therein;
L. Tiator, D. Drechsel, O. Hanstein, S.S. Kamalov, S.N. Yang, Nucl. Phys. A 689 (2001) 205–c214.
[62] K.M. Watson, Phys. Rev. 95 (1954) 228–236;
M. Ross, Phys. Rev. 94 (1954) 454–460.
[63] Numerical Algorithms Group Ltd., Wilkinson House, Jordan Hill Road, Oxford OX2-8DR, UK. <http://www.nag.co.uk//>.
[64] K. Deb, Multi-objective Optimization using Evolutionary Algorithms, Wiley, New York, 2002;
L. Davis, Handbook of Genetic Algorithms, Van Nostrand Reinhold, New York, 1991.
[65] V. Bellini et al., Nucl. Phys. A 646 (1999) 55–66.
[66] C. Fernández-Ramírez, E. Moya de Guerra, J.M. Udías, Phys. Rev. C., to be published. <arXiv:nucl-th/0601037/>.
[67] H.W.L. Naus, J.H. Koch, J.L. Friar, Phys. Rev. C 41 (1990) 2852–2864, and references therein;
J.C. Bergstrom, Phys. Rev. C 44 (1991) 1768–1783.
[68] C. Fernández-Ramírez, Diploma Thesis (unpublished), Universidad Complutense de Madrid, 2003.
[69] P.J. Bussey et al., Nucl. Phys. B 159 (1979) 383–396;
P.J. Bussey et al., Nucl. Phys. B 169 (1980) 403–414;
I.S. Barker, A. Donnachie, J.K. Storrow, Nucl. Phys. B 347 (1975) 347–356.
[70] D. Dutta, H. Gao, T.-S.H. Lee, Phys. Rev. C 65 (2002) 044619.
[71] G.F. Chew, M.L. Goldberger, F.E. Low, Y. Nambu, Phys. Rev. 106 (1957) 1345–1355;
F.A. Berends, A. Donnachie, D.L. Weaver, Nucl. Phys. B 4 (1967) 1–53.
[72] R.A. Arndt, R.L. Workman, Z. Li, L.D. Roper, Phys. Rev. C 42 (1990) 1864–1866.